You might find this additional info useful...

Supplementary material for this article can be found at:
http://jn.physiology.org/http://jn.physiology.org/content/suppl/2012/04/27/jn.00098.2011.DC1.html

This article cites 90 articles, 20 of which you can access for free at:
http://jn.physiology.org/content/108/4/956.full#ref-list-1

Updated information and services including high resolution figures, can be found at:
http://jn.physiology.org/content/108/4/956.full

Additional material and information about *Journal of Neurophysiology* can be found at:
http://www.the-aps.org/publications/jn

This information is current as of August 30, 2012.

Pitfalls in the dipolar model for the neocortical EEG sources

Jorge J. Riera,[1] Takeshi Ogawa,[1]* Takakuni Goto,[1]* Akira Sumiyoshi,[1] Hiroi Nonaka,[1] Alan Evans,[2] Hiroyoshi Miyakawa,[3] and Ryuta Kawashima[1]

[1]*Institute of Development, Aging and Cancer, Tohoku University, Sendai, Japan;* [2]*McConnell Brain Imaging Centre, Montreal Neurological Institute, McGill University, Montreal, Quebec, Canada;* and [3]*School of Life Sciences, Tokyo University of Pharmacy and Life Sciences, Tokyo, Japan*

Riera JJ, Ogawa T, Goto T, Sumiyoshi A, Nonaka H, Evans A, Miyakawa H, Kawashima R. Pitfalls in the dipolar model for the neocortical EEG sources. *J Neurophysiol* 108: 956–975, 2012. First published April 25, 2012; doi:10.1152/jn.00098.2011.—For about six decades, primary current sources of the electroencephalogram (EEG) have been assumed dipolar in nature. In this study, we used electrophysiological recordings from anesthetized Wistar rats undergoing repeated whisker deflections to revise the biophysical foundations of the EEG dipolar model. In a first experiment, we performed three-dimensional recordings of extracellular potentials from a large portion of the barrel field to estimate intracortical multipolar moments generated either by single spiking neurons (i.e., pyramidal cells, PC; spiny stellate cells, SS) or by populations of them while experiencing synchronized postsynaptic potentials. As expected, backpropagating spikes along PC dendrites caused dipolar field components larger in the direction perpendicular to the cortical surface (49.7 ± 22.0 nA·mm). In agreement with the fact that SS cells have "close-field" configurations, their dipolar moment at any direction was negligible. Surprisingly, monopolar field components were detectable both at the level of single units (i.e., −11.7 ± 3.4 nA for PC) and at the mesoscopic level of mixed neuronal populations receiving extended synaptic inputs within either a cortical column (−0.44 ± 0.20 μA) or a 2.5-m³-voxel volume (−3.32 ± 1.20 μA). To evaluate the relationship between the macroscopically defined EEG equivalent dipole and the mesoscopic intracortical multipolar moments, we performed concurrent recordings of high-resolution skull EEG and laminar local field potentials. From this second experiment, we estimated the time-varying EEG equivalent dipole for the entire barrel field using either a multiple dipole fitting or a distributed type of EEG inverse solution. We demonstrated that mesoscopic multipolar components are altogether absorbed by any equivalent dipole in both types of inverse solutions. We conclude that the primary current sources of the EEG in the neocortex of rodents are not precisely represented by a single equivalent dipole and that the existence of monopolar components must be also considered at the mesoscopic level.

electroencephalogram; neocortex; multipolar current sources; inverse problem

THE DIPOLAR MODEL, used by generations of neuroscientists to represent the current sources of the electroencephalogram (EEG) in humans (Niedermeyer and Lopes da Silva 1987; Nunez and Srinivansan 2006; Plonsey 1969; Walter and Walter 1949), has roots in early interpretations by Adrian and Matthews (1934) about the origin of the Berger rhythm (i.e., the alpha rhythm). These authors suggested that the cortical electric potentials formerly observed by Berger (1929) were caused by electrical sources close to the brain surface with a polarity inversion in the axis perpendicular to it. The existence of dipole-like field distributions with axes parallel to the cortical surface was later suggested by Beevers (1944), with confirmations for the kappa rhythm (Kennedy et al. 1948) and the epileptic focal seizures (Gumnit and Takahashi 1965). This model, which eventually gained popularity in many other emerging applications of EEG (e.g., sleep: Brazier 1949; epilepsy: Gumnit and Takahashi 1965), was originally formulated by Shaw and Roth (1955) in terms of the electric field theory. The feasibility of estimating such dipolar sources from actual EEG data was successfully tested in several preliminary experiments (Henderson et al. 1975). This methodology then became one of the most remarkable breakthroughs in the EEG renaissance period that started with the substitution of polygraphs (i.e., ink-writing amplifiers) and cathode-ray oscilloscopes by the digital EEG amplifiers in the 1980s, a situation that happened to occur almost at the same time that personal computers smashed IBM punch cards. In particular, parametric source analysis methods based on least-squares estimation of moving (Schneider 1972) and spatiotemporal (Scherg and Von Cramon 1985) dipole models were at that time, and even are now (Mosher et al. 1992; Xu et al. 2004), very helpful to localize current sources inside the brain and to segregate them in circumstances of simultaneously activate regions. Furthermore, the concept of current dipole density underlies most of the modern imaging methods (Baillet et al. 2001), e.g., beamforming/MUSIC approaches and distributed source models. With the development of chronically implanted electrodes in humans during the 1950s to treat psychiatric patients through a frontal leucotomy (Sem-Jacobsen et al. 1955) and also to characterize epileptic seizures (Abraham and Ajmone-Marsan 1958), it was possible to examine in situ the biophysical foundations of the EEG dipolar model. During this early period, further comparative evaluations were also made possible with the help of animal models.

For the cerebral cortex, researchers first focused on clarifying the strength and extension of the actual current dipoles. In a pioneer work, Cooper et al. (1965) concluded that a synchronous activation of a cortical area of 6 cm² is required to produce observable signal in the human EEG data, although subsequent studies showed that a recruitment of larger areas might be necessary (Ebersole 1997, 2000; Tao et al. 2005). More contemporary studies using simultaneous magnetoencephalographic (MEG) and subdural EEG recordings revealed that just an area of ~4 cm² of synchronized cortical activity is necessary to produce an observable MEG signal (e.g., alpha

* T. Ogawa and T. Goto contributed equally to this work.

Address for reprint requests and other correspondence: J. J. Riera, Dept. of Functional Brain Imaging, Institute for Development, Aging and Cancer, Tohoku Univ., 4-1 Seiryocho, Aobaku, Sendai 980-8575, Japan (e-mail: riera@idac.tohoku.ac.jp).

rhythm: Chapman et al. 1984; epileptogenic activity: Mikuni et al. 1997; Oishi et al. 2002). The first estimation of the cortical current density is attributable to bipolar recordings from the prepyriform cortex of adult anesthetized cats (Freeman 1959), which clearly showed the existence of voltage differences of up to 1.5 mV between electrodes that were 1.5 mm apart. Note that in this preliminary study the electrodes were inserted perpendicular to the cortical surface until a maximal dipolar field configuration was evoked by electrical stimulation of the olfactory bulb. A second estimation emanated from extracellular potentials of spike-wave responses in the precruciate cortex in cats that were evoked by stimulation of the thalamus (Pollen 1969). This author found voltage gradient along the cortical laminas of up to $400-450$ μV/mm. Taking into account these observations and timely estimations of the cortical conductivity (e.g., rabbits: 2.73–3.62 mS/cm, Ranck 1963; cats: 1.66–1.96 mS/cm, Li et al. 1968), it was possible through the use of the methodology proposed by Humphrey (1968) to obtain ranges ($100-250$ nA/mm^2) for the typical transcortical current densities (Freeman 1975; Pollen 1969), which remain valid to this day (Baillet et al. 2001). The strengths and spatial extensions of cortical dipoles were in agreement with estimations obtained from EEG and MEG data (10–100 nA·m: Bowyer et al. 1999; Cohen and Cuffin 1983; Chapman et al. 1984; Jones et al. 2007, 2009). In addition, these values were compatible with later predictions of the transcortical current density from anatomophysiological considerations (Hämäläinen and Ilmoniemi 1984; Hämäläinen et al. 1993; Hari and Ilmoniemi 1986).

Understanding the laminar/neuronal substrates of the actual cortical dipoles constituted a second issue of interest in the past. In fact, the existence of cortical dipoles was initially supported by the observation of phase reversals between an electrode lying on the cortical surface and another in the white matter beneath the cerebral cortex (Calvet and Scherrer 1961). Later, Lopes da Silva and van Leeuwen (1977) provided convincing evidence for a phase reversal (i.e., 180° about 1,100 μm from the cortical surface) in the case of alpha rhythm recordings from unrestrained dogs. Such observations were consistent with studies that explained the spontaneous EEG by the succession/mingling of the activities of different types of dipoles distributed along the cortical layers (cats: Calvet et al. 1964; rabbits: Rappelsberger et al. 1982), with the pyramidal cells (PCs) at both the infra- and supragranular layers being the most important contributors (Di et al. 1990; Kraut et al. 1985). Even so, other studies claimed that the concept of phase reversal was only valid to a limited extent (Gumnit and Takahashi 1964; Petsche et al. 1977). In particular, it was pointed out that true mirror images were hardly observed in practice, and when they were, the temporal coherence estimates between the corresponding sources and sinks were very low. In many contemporary studies, current source density (CSD) distributions inside the neocortex have been examined with much better accuracy with the help of both high-resolution silicon-based microelectrodes arrays and advanced mathematical constructs. Indeed, the existence of unbalanced currents sources with no clear reversals in the laminar polarity is also suggested from CSD distributions in the somatosensory (Ahrens and Kleinfeld 2004; Di et al. 1990; Higley and Contreras 2007; Mégevand et al. 2008), motor (Ahrens and Kleinfeld 2004), visual (Lakatos et al. 2008), and auditory cortices (Lakatos et al. 2007) for a variety of experimental paradigms. As an alternative explanation for these unbalanced CSD distributions, some researchers have presupposed that additional current source/sink distributions with counterpart polarity might exist along the tangential directions to the cortical surface (e.g., Nunez P, personal communication). Likewise, even though shifted dipoles were initially associated with backpropagating action potentials in layer V PCs (Buzsáki and Kandel 1998), exact balanced CSD patterns are not that evident from estimation with the highest spatial resolutions (Bereshpolova et al. 2007).

Lastly, biophysical models of single neurons were used from the beginning to establish the neuronal foundations of the extracellular potentials and hence of the EEG data. For instance, on the basis of the extracellular potentials generated by an axon undergoing an action potential, Lorente de Nó (1947) proposed the concept of "open" and "closed" field configurations for remote EEG observations. In this initial work, the extracellular potentials were calculated by approximating each cell by point sources with strengths determined by the electric currents flowing across the corresponding cell membrane patches. Succeeding theoretical studies determined the extracellular electric potentials generated by synaptic inputs to the somas of either single neurons (Rall 1962) or populations of them (Klee and Rall 1977). As a result of having the dendrites organized along a particular direction, PCs have been classified as open-field neurons. In contrast, as a consequence of their radially symmetric dendrites, spiny stellate (SS) cells are thought to have a closed-field configuration. These previous studies are based on the quasi-static approach of the electric fields in the brain tissues (Plonsey and Heppner 1967) and the compartmental models of neurons (Johnston and Wu 1994; Rall 1962). Original compartmental models of neurons resulted from *1*) the introduction of dimensionless distance/time variables in the cable equation, *2*) the linearization of ionic current kinetics inside each dendritic branch, and *c*) the use of the equivalent cylinder theorem for dendritic trees (i.e., determining input resistances for branches and dendritic attenuation effects). The latter has been formulated on the basis of three main conditions: *1*) the cumulative electrotonic length condition, *2*) the 3/2 power law at every branch point condition, and *3*) the termination condition. More recently, Holt and Koch (1999) proposed the line source model, which simplifies the dendrites by lines with zero widths. The cable equation constitutes the standard biophysical model underlying these previous studies, which is based explicitly on Kirchhoff's current law. Therefore, the total current flowing across the whole cell membrane must be zero at each time instant, and as a consequence there will be no unbalanced currents sources inside the brain at a microscopic level.[1] This assumption has led us to reject, since the very beginning, the existence of monopolar current source components in any mesoscopic volume inside the neocortex (Llinás and Nicholson 1974; Nunez 1981). More contemporaneous biophysical models for the genesis of the extracellular potentials are also built on the basis of equivalent assumptions and theoretical frameworks (Gold et al. 2006, 2007; Jones et al. 2007; Murakami and Okada 2006; Pettersen

---

[1] Definitions: *1*) microscopic level, from a membrane patch to a single neuron; *2*) mesoscopic level, from an anatomic microcolumn to a group of functional columns, e.g., the barrel field; and *3*) macroscopic level, from a single brain area to the entire head.

and Einevoll 2008). However, Bédard and Destexhe (2009) suggested recently the existence of ionic diffusion effects across the cellular membranes, which may be larger than any ohmic effect. These authors claimed that ionic diffusion is responsible for the frequency dependence of the electric conductivity/permittivity and provided a new explanation for the $1/f$ noise scaling in the local field potentials (LFP). Dehghani et al. (2011) found that the significant differences in the scaling of the power spectral density for the EEG and MEG could be also explained by considering high dispersive effects in the brain tissues.

In this report, we recapitulate the concept of a cortical dipolar model in the light of recent advances both in technologies for electrophysiological recordings and in methods for the analysis of cortical CSD. First, using a customized three-dimensional (3-D) probe, we recorded LFP and unit activity from the barrel cortex of Wistar rats undergoing both single and whole whisker stimulations at 1 Hz. We recently introduced a method (Goto et al. 2011) to estimate the volumetric CSD associated with both backpropagating action potentials in individual cells and population synaptic activities evoked by the whisker deflections. In both cases, we found important dipolar and quadrupolar contributions but also the existence of unbalanced current sources in the neocortex. To verify the impact of such local current unbalance in the EEG, and of any higher order multipoles as well, we used multiscale electrophysiological data recorded from Wistar rats. These multiscale data consist of high-density skull EEG recordings concurrently observed with laminar LFP through a silicon-based probe implanted in the barrel field while multiple whiskers were deflected at two different frequencies (1 and 3 Hz). In this case, the analysis of mesoscopic CSD was performed using the inverse CSD (iCSD) method (Pettersen et al. 2006), and the results were used to estimate the multipolar moments for each stimulus frequency in the recorded barrel region. The dynamics of the equivalent macroscopic dipole in the barrel cortex were estimated from both a least-squares dipolar fitting (Jones et al. 2007) and the surface low-resolution electromagnetic tomography (LORETA) type of inverse solution (Riera et al. 2000). The classical surface LORETA is also based on a dipolar representation of the cortical current sources. The mesoscopic multipolar moments were normalized and then used, as known loadings in a linear regression analysis, to predict the time courses of the estimated EEG dipole for the whole barrel field.

MATERIALS AND METHODS

The experiments were performed with the approval of the Animal Care Committee at Tohoku University.

Animal preparation. Thirteen Wistar rats (8 wk, male) were anesthetized with urethane (1.2 g/kg). For each rat, the scalp was partially removed, leaving a large portion of the skull exposed. A craniotomy of 2 mm in diameter was made on the right primary barrel cortex (Riera et al. 2010a). Two screws, used as a reference and ground for the intracranial electric recordings, were attached to the skull around the right mastoid. HEPES-buffered and Ca^{2+}-free artificial cerebral spinal fluid (aCSF: 150 mM NaCl, 2.5 mM KCl, 1 mM $MgCl_2 \cdot 6H_2O$, 10 mM HEPES, and 10 mM glucose, pH adjusted to 7.4 with Tris base) was applied to the exposed cortex, after which a small patch of dura matter from the top of the observation site was carefully removed. We prepared the rats for two types of experiments: *1*) vol-

umetric extracellular recordings and *2*) concurrent EEG and LFP recordings.

For volumetric extracellular recordings ($n = 4$), we designed a 3-D silicon-based probe (NeuroNexus Technologies; Fig. 1*A*) to record LFP from 128 locations inside 2.02 mm^3 of cortical tissue. This probe consists of a regular and parallel array of four laminar probes with iridium oxide microelectrodes (i.e., area 177 μm^2, intermicroelectrode intervals 200 μm), which were separated by a distance of 400 μm. This arrangement results in a 4 × 4 regular grid of shanks covering, after insertion, a total cortical area of 1.44 mm^2 (i.e., several barrels). The 3-D probe was perpendicularly inserted in the barrel cortex and the craniotomy filled with nonconductive paraffin oil (Nacalai tesque).

For concurrent EEG and LFP recordings ($n = 9$), a gel with a conductivity value adjusted to simulate that of the actual rat's skull (0.13 ± 0.08 mS/cm) was applied on the craniotomy. By means of a fine brush, we applied a thin layer of this conductive gel to the exposed skull with a twofold intention: to improve the conductance at the electrode/skull interface and to keep the bone from drying throughout the experiment. A homemade EEG mini-cap (Fig. 1*B*, *top*) was set on the rat's head by firmly attaching fixed-aluminum bars (1 on the nasal channel and 2 posterior to the interaural line) to the skull using self-etching adhesive resin cement (Tokuyama Dental). Details about the EEG mini-cap as well as a method to achieve low electrode impedances are provided in Riera et al. (2010b). A similar EEG mini-cap was used recently by Sumiyoshi et al. (2011) to perform high-resolution EEG recording inside a 7T MRI scanner. After the EEG mini-cap fixation, a silicon-based probe (NeuroNexus Technologies), which consists of a linear shank with an array of iridium oxide microelectrodes (i.e., area 177 μm^2, intervals 50 μm) was perpendicularly inserted at different depths into the cerebral cortex through an available hole in the EEG mini-cap (i.e., probe area). Arbitrarily, we employed silicon-based probes with either 16 (short probe, 5 rats) or 32 microelectrodes (long probe, 4 rats). The impedance of the microelectrodes in the probe ranges within the interval of 0.7–0.9 MΩ. The impedance for all EEG electrodes was less than 50 kΩ in all experiments (Fig. 1*B*, *bottom*), as determined using BrainVision Recorder software (Brain Products). For the EEG recordings, the reference and ground electrodes (SEE203; GE-Marquette Medical Systems) were placed on the right and left ear lobes, respectively.

In all experiments, the penetration length and insertion angle of silicon-based probes were accurately monitored/corroborated through a micromanipulator's control system (SM5; Luigs & Neumann) and the bregma stereotaxic coordinates (Paxinos and Watson 2007).

Electrophysiological recordings. High-resolution intracranial electrical recordings were obtained using amplifiers at 25 kHz (PZ2; Tucker and Davis Technologies) connected by an optical fiber to signal processing unit comprising 8 parallel DSP (RZ2; Tucker and Davis Technologies) and by coaxial cable to a preamplifiers located inside acute 18-bit hybrid head stages. Extracellular potentials were collected online using a logic/symbolic programming language supported by the signal processing unit (OpenEx software; Tucker and Davis Technologies). To obtain LFPs from the raw data, we applied a Butterworth band-pass filter with cutoff frequency set between 1 and 500 Hz. Event-related LFPs, corresponding to whisker deflections, were calculated by averaging stimulus-locked LFP responses over a large number of trials (>100). To detect unit activity, a band-pass filter with cutoff frequency set between 500 Hz and 8 kHz was also applied to the raw data. We then extracted neuronal spikes by negative edge detection with a threshold of 4 times the standard deviation and 1.5 ms of dead time. Twenty samples (i.e., 8 samples prior and 12 samples posterior to the minima) of the detected spikes were used for classification. The spikes at each microelectrode were classified into putative PCs and SS cells (Goto et al. 2011; Ogawa et al. 2011). The spike time events were used as the triggers to compute spike-related potentials (SRPs) for each particular classified cell. EEG recordings (32 channels) were obtained using commercial EEG amplifiers (BrainAmp MR; Brain Products), with input impedance of 10 MΩ,
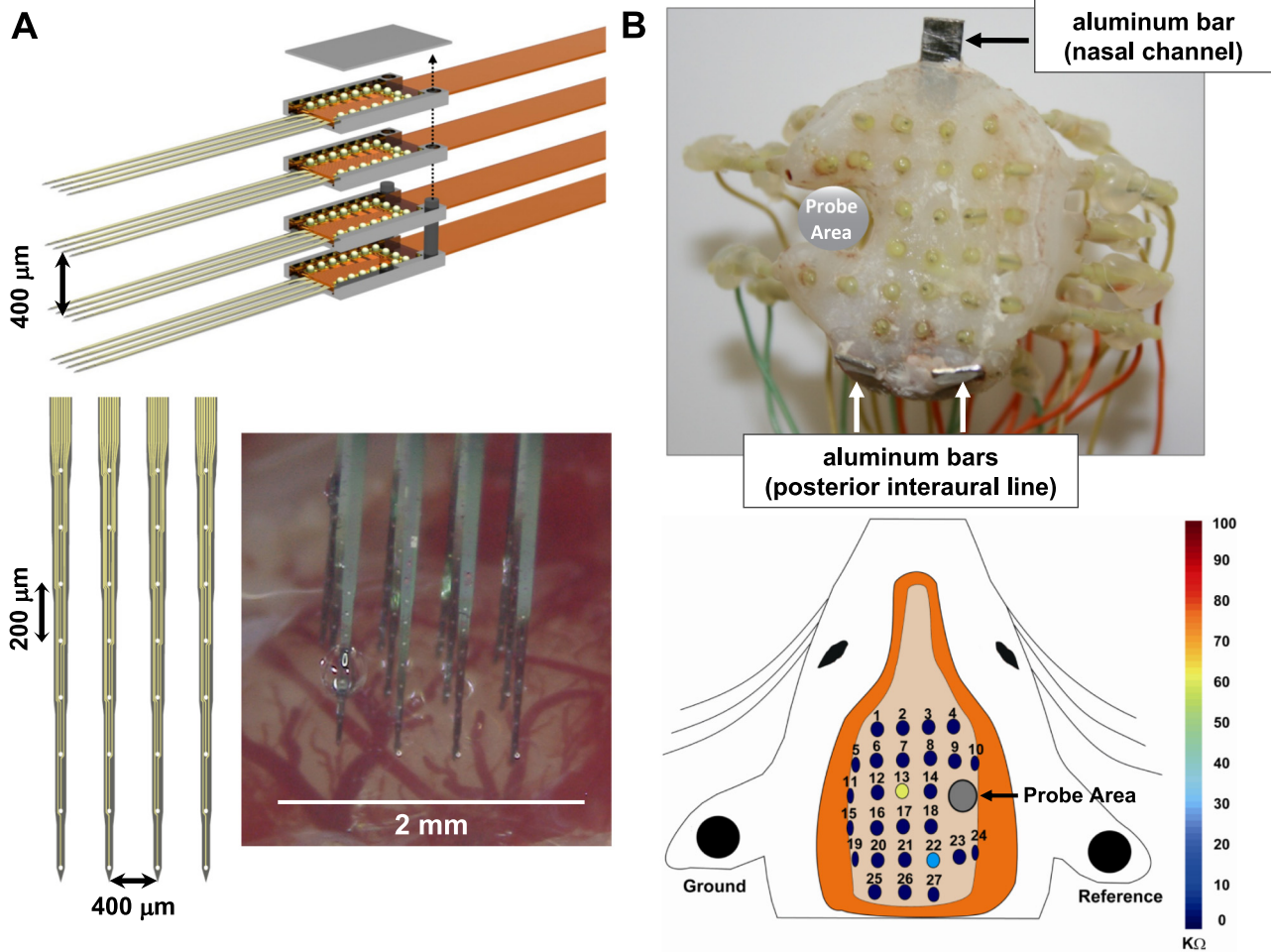
Fig. 1. Three-dimensional probe and electroencephalogram (EEG) mini-cap. *A*: customized design of the 3-dimensional probe (courtesy of NeuroNexus). The picture of the 3-dimensional probe was taken just before insertion in the somatosensory barrel cortex with a digital microscope (KH-1300; HIROX, Tokyo, Japan). *B*: view from the bottom of the EEG mini-cap (*top*). The EEG mini-cap is created from melted plastic poured into a mold. In the mold (made from plaster), stainless steel needles were perpendicularly situated in those positions defined for the electrodes. The needles were covered with hard plastic tubes (1.5 mm) that were finally fixed to the melted plastic. A hole was created for intracranial local field potential (LFP) recording (probe area). Three aluminum bars were also fused with the plastic. These aluminum bars are needed to firmly attach the EEG mini-cap to the skull. The EEG mini-cap has sliding silicon tubes (1.4 mm) positioned inside the hard plastic tubes. The silicon tubes, which are filled with a conductive gel, contain platinum wires. The actual impedance values of the EEG electrodes for this particular experiment, as determined using BrainVision Recorder software (Brain Products), are shown using color coding (*bottom*).

input noise at 2 μVpp (peak-to-peak voltage), in-phase suppression at >90 dB, and signal range/resolution of ±16 mV/500 nV. The EEG digitalized signal was band-pass filtered online using software-controlled digital filters, i.e., the lower and upper cutoffs were set at 0.016 and 1,000 Hz, respectively. An equivalent large number of single trials were used to estimate the event-related EEG signals from stimulus-locked EEG responses.

Whisker stimulation protocol. We used both a single and a whole whisker deflection protocol to stimulate the left vibrissae system of the rats. In both cases, the whiskers were shortened to 1 cm in length and deflections were carried out from the rostral to the caudal direction. Single whiskers were deflected by a piezoelectric bimorph actuator (TAYCA, Osaka, Japan) that was controlled by a piezodriver (PCD-001; General Photonics). The deflection angle, frequency, and interval for each stimulus were set to 7.2°, 1 Hz, and 100 ms, respectively. Whole whiskers were deflected by short (10 ms in duration) air puffs. The needle tip used for stimulation was placed ~2 cm away from the rat's jaw and approximately parallel to its snout. The air puffs were generated from a high-pressure air tank controlled by a pneumatic picopump (PV830; World Precision Instruments) at a pressure of 15 psi. The frequencies of air-puff stimulation were 1 and 3 Hz. A program in Matlab (version 7.5.0.342, R2007b; The Math-

Works) was used to automatically control the operating devices (i.e., RZ2, BrainAmp MR, PCD-001, and PV830) through a multiple input/output analog-to-digital converter (PCI-6259; National instruments) as well as to generate the desired triggers for the stimulation and recording devices (i.e., to perform off-line analyses).

MRI anatomic imaging. High-resolution T1-weighted anatomic images were acquired on a 7T MRI scanner with a maximum gradient of 300 mT/m (70/16 Pharmascan; Bruker BioSpin, Karlsrühe, Germany) using a 38-mm rat brain quadrature resonator for radiofrequency transmission and reception. The rats were placed onto a head holder comprising a tooth bar. The animals were kept warm with water circulating at 37°C. Volumetric images were acquired using a T1-weighted 3D RARE sequence with fat suppression, 300/8.5-ms TR/TE, RARE factor 4, 100-kHz spectral bandwidth, 8 averages, 3.4 × 3.4 × 3.84-cm³ field of view, 256 × 256 × 128 image matrix, and 125 × 125 × 300-μm³ voxel resolution. The T1-weighted anatomic images (Supplemental Video 1) were obtained 2 days before to the electrophysiological experiment, with a total acquisition time of 4 h and 5 min. (Supplemental data for this article is available online at the *Journal of Neurophysiology* website.) During MRI experiments, the rats were anesthetized with isoflurane (0.5–1.5%) mixed in pure oxygen.

Immunostaining. Coronal sections (100 μm thick) of the entire barrel cortex were obtained from the postmortem fixed brains of those rats used for the concurrent EEG and LFP experiments. In contrast, the rat brains were sectioned tangentially to the cortical surface for the volumetric LFP experiment. To reveal the barrels, sections were treated with 3,3′-diaminobenzidine (Sigma) and cytochrome *c* oxidase from horse heart (Sigma) (Riera et al. 2010a). Fluorescent Nissl staining of the brain sections was additionally performed to determine the relative position of the silicon-based probe with respect to the cortical layers. Immunostained images were obtained using an upright fluorescent microscope (SZX16; Olympus). To colocalize the silicon-based probe and the layers/barrels, shanks were submerged before insertion in a solution containing lipophilic neuronal tracer carbocyanine (DiI; Invitrogen).

CSD analysis. To analyze the distributions of diminutive electric current sources $s = -\sigma\nabla^2\varphi$ (in μA/mm^3) inside a mesoscopic region (i.e., a cortical barrel), we used the volumetric CSD method (vCSD, a Matlab code developed in our laboratory; Goto et al. 2011) and the inverse CSD method (iCSD; iCSDplotter software, version 0.1.1, http://bebiservice.umb.no/projects-public/cnsweb/wiki/Miscellaneous/Downloads; Pettersen et al. 2006).

The parameters used in the vCSD method were *1)* the intergrid distance Δ, which was 50 μm, and *2)* the radial/tangential conductivities and radii for all cortical layers, which were previously estimated by Goto et al. (2010) for the somatosensory cortex of adult Wistar rats. We applied the average reference operator (Pascual-Marqui 1999) to the Green's function matrices, event-related LFPs, and SRPs to remove undesirable signals from the reference electrode (Bertrand et al. 1985). The parameters used in the iCSD method were *1)* the disk diameter *d* for the sources (i.e., the barrels), which was 0.5 mm, *2)* the standard deviation for the Gaussian filter, which was 50 μm, *3)* the thickness of the cortical columns for the barrel cortex *l*, which was 2 mm, and *4)* the mean electric conductivity σ (homogenous media) for brain tissues, which was 3 mS/cm.

For both methods, we did not use boundary conditions (i.e., free electric potentials). To estimate the laminar/volumetric current sources associated with particular neuronal activities, we applied the iCSD/vCSD method to the event-related LFPs and SRPs obtained in each experiment. The mathematical definitions of multipolar moments [e.g., monopoles, $m(t)$; dipoles, $\vec{\mathbf{d}}(t)$; and quadrupoles, $\overset{\leftrightarrow}{\mathrm{Q}}(t)$] from the volume current sources *s* in a volume of interest V are given by the following equations:

$$m(t) = \int_{V} s(\vec{r}, t)d\vec{r}^3$$

$$\vec{\mathbf{d}}(t) = \int_{V} s(\vec{r}, t)(\vec{r} - \vec{r}_m)d\vec{r}^3 \qquad (1a)$$

$$\overset{\leftrightarrow}{\mathrm{Q}}(t) = \int_{V} s(\vec{r}, t)(\vec{r} - \vec{r}_m)(\vec{r} - \vec{r}_m)d\vec{r}^3$$

In particular, for the iCSD method, these equations take a simplified form:

$$m_z(t) = \pi\left(\frac{d}{2}\right)^2 \int s(z, t)dz$$

$$d_z(t) = \pi\left(\frac{d}{2}\right)^2 \int s(z, t)(z - z_m)dz \qquad (1b)$$

$$Q_z(t) = \pi\left(\frac{d}{2}\right)^2 \int s(z, t)(z - z_m)^2 dz$$

Assuming the barrel columns are perfect cylinders, their volumes V = $\pi(d/2)^2 l$ would be 0.39 mm^3. The vector $\vec{r}_m$ indicates the center of gravity of the cortical column, and the value z_m stands for its respective laminar coordinate. The *z*-axis is defined in the direction perpendicular to the neocortex, with positive and negative values

toward the supragranular and infragranular layers, respectively. The integrals above were evaluated numerically using a trapezoidal method, where each subinterval corresponds to a particular grid point in the corresponding CSD method.

EEG forward/inverse problem. To relate the observed electric potentials and their causing current source configuration inside the brain, the rat's head was modeled as an isotropic and piecewise homogeneous volume conductor. There was no skin tissue in the area where the electrodes were located; hence, the brain and the skull constituted the main tissue compartments. The positions of the electrodes were defined from pictures taken during the experiments and landmarks on the 3-D-reconstructed T1-weighted anatomic references (Supplemental Video 2). The skin tissue was ignored because it was removed above the interaural axial plane (red dashed line). Realistic shapes for the surfaces limiting the above-mentioned tissue compartments were segmented and triangulated (Supplemental Video 2). We employed 642 triangles per surface, i.e., 1,280 vertexes. The conductivities used for brain and skull compartments were 2.9 mS/cm (Nunez and Srinivansan 2006) and 0.13 mS/cm (Oostendorp et al. 2000), respectively.

In general, an electric potential $v(\vec{r}_e, t)$ (μV) at any position $\vec{r}_e$ on the skull produced by a continuous field of microscopic electrical sources $I(\vec{r}, t)$ (dimensions: $I \sim \mu$A/mm^3) inside the brain *R* can be represented by an inhomogeneous Fredholm integral equation of the second kind (*Eq. 2*), with the secondary currents $\vec{\mathbf{j}}_k(I, \vec{r}) = (\sigma_{k+1} - \sigma_k)v_k(I, \vec{r})\vec{\mathbf{n}}_k(\vec{r})/\Delta l$ defined for each elemental volumetric shell Ω_k (i.e., the surface S_k of thickness $\Delta l \rightarrow 0$). The symbol σ_k denotes the conductivity of the *k*th compartment (i.e., brain, skull), and $\vec{\mathbf{n}}_k(\vec{r})$ is the normal vector to the surface S_k at location $\vec{r}$. The current source can be interpreted in terms of the electrical charge density as $\rho(\vec{r}, t) \rightarrow I(\vec{r}, t)/\sigma$. The theoretical foundations and numerical strategies for calculating surface potentials $v_k(I, \vec{r})$ are given in Hämäläinen and Sarvas (1989).

$$4\pi\sigma v(\vec{r}_e, t) = 4\pi\sigma v_0(\vec{r}_e, t) + \sum_k \int_{\Omega_k} \vec{\mathbf{j}}_k(I, \vec{r}) \cdot \nabla\left(\frac{1}{|\vec{r}_e - \vec{r}|}\right)d\vec{r}^3 \qquad (2a)$$

$$v_0(\vec{r}_e, t) = \frac{1}{4\pi\sigma}\int_R \frac{I(\vec{r}, t)}{|\vec{r}_e - \vec{r}|}d\vec{r}^3 \qquad (2b)$$

Let us assume

$$I(\vec{r}, t) = \begin{cases} s(\vec{r}, t) & \vec{r} \in V \\ 0 & \vec{r} \notin V \end{cases},$$

where V is a specific mesoscopic volume centered at $\vec{r}_m$. If the observation site $\vec{r}_e$ is far enough from the center $\vec{r}_m$, then $v_0(\vec{r}_e, t)$ can be written as a function of the multipolar moments:

$$v_0(\vec{r}_e, t) = \frac{1}{4\pi\sigma}\left[\frac{m(t)}{|\vec{r}_e - \vec{r}_m|} + \vec{\mathbf{d}}(t) \cdot \nabla_{\vec{r}_m}\left(\frac{1}{|\vec{r}_e - \vec{r}_m|}\right) \right.$$
$$\left. + \frac{1}{2}\overset{\leftrightarrow}{\mathrm{Q}}(t) : \nabla \nabla_{r_m}\left(\frac{1}{|\vec{r}_e - \vec{r}_m|}\right) + \cdots \right] \qquad (3)$$

The scalar product $\vec{\mathbf{a}} \cdot \vec{\mathbf{b}}$ and the tensor contraction $\overset{\leftrightarrow}{\mathrm{A}} : \overset{\leftrightarrow}{\mathrm{B}}$ are defined in Jerbi et al. (2002). Generalizing this concept to include contributions from all cortical columns, with the proper substitution of multipolar moments by their respective densities in a macroscopically continuous sense, and also from other mesoscopic regions of the brain, we obtain

$$v_0(\vec{r}_e, t) = \frac{1}{4\pi\sigma}\left[\int_R \frac{m(\vec{r}, t)}{|\vec{r}_e - \vec{r}|}d\vec{r}^3 + \int_R \vec{d}(\vec{r}, t)\cdot\nabla_{\vec{r}}\left(\frac{1}{|\vec{r}_e - \vec{r}|}\right)d\vec{r}^3\right.$$
$$\left. + \int_R \frac{1}{2}\overleftrightarrow{Q}(\vec{r}, t):\nabla\nabla_{\vec{r}}\left(\frac{1}{|\vec{r}_e - \vec{r}|}\right)d\vec{r}^3 + \cdots\right] \quad (4)$$

Under the assumption of the dipolar model, the final EEG forward problem is represented by *Eqs. 2a* and *5*:

$$v_0(\vec{r}_e, t) = \frac{1}{4\pi\sigma}\int_R \vec{d}(\vec{r}, t)\cdot\nabla_{\vec{r}}\left(\frac{1}{|\vec{r}_e - \vec{r}|}\right)d\vec{r}^3 \quad (5)$$

EEG recordings $v^e_{t_k} = v(\vec{r}_e, t_k) - v(\vec{r}_r, t_k)$ constitute discrete observations in time t_k ($k = 0, \ldots, N_T$) and space $\vec{r}_e$ ($e = 1, \ldots, N_e$), which are always contaminated with observational noise $e^e_{t_k}$ and measured with respect to a common reference electrode $\vec{r}_r$. For biophysical reasons (Baillet et al. 2001), it is feasible to assume that most of the EEG signal comes from the cortical surface. Therefore, it is worthwhile to set $\vec{d}(\vec{r}, t)$ different from zero only on the cortical surface. The dipolar moment has been assumed to originate from postsynaptic currents caused mainly by the activation of PCs perpendicular to the cortical surface (Hämäläinen et al. 1993; Okada et al. 1997). Therefore, the vector current source can be written as $\vec{d}(\vec{r}, t) = \vec{\mu}(\vec{r})d(\vec{r}, t)$, with $\vec{\mu}(\vec{r})$ and $d(\vec{r}, t)$ representing the normal direction to Γ (from the white matter to the external brain surface) and the time-varying dipole amplitude, respectively. The EEG forward problems can be finally written as generalized linear convolutions (*Eq. 6*), with kernel $h(\vec{r}_e, \vec{r})$.

$$v^e_{l_k} = \int_\Gamma h(\vec{r}_e, \vec{r})d(\vec{r}, t_k)d\vec{r}^2 + e^e_{t_k} \quad (6)$$

The kernel for the EEG forward problems can be defined from *Eqs. 3–5* in Hämäläinen and Sarvas (1989), with particular considerations for the electric potential in the infinite homogeneous medium (*Eq. 5*). This represents a scalar boundary element method incorporating deflections and an isolated problem approach. This boundary element method was implemented in Matlab. The code is available on request from the corresponding author. The numerical evaluation of the kernel in *Eq. 6*, for a particular electrode, on the triangulated cortical surface of an individual rat is shown in Supplemental Video 2. In this report, the EEG forward problem is used to perform the equivalent dipole fitting by a least-squares strategy (Jones et al. 2007) and the surface LORETA inverse solution (Riera et al. 2000).

RESULTS

Because the vibrissae system in rodents is very well documented (Petersen 2007), electrophysiological data recorded from rats under a whiskers stimulation paradigm will be of great utility to understand the nature of the neocortical current sources on the mesoscopic scale, as well as to quantify the relationships they keep with the macroscopic data.

vCSD analysis. In a first experiment, we applied the vCSD method to estimate from 3-D recordings of extracellular potentials the intracortical multipolar moments generated either by spiking neurons (i.e., PC, SS) or during their synchronized population postsynaptic activity. PCs have been considered the primary sources of the LFP, as well as EEG, whereas SS cells are assumed to produce no resultant extracellular electric potentials due to their closed-field configuration. As a result of technological limitations in the past, a precise validation of these properties through a quantification of the actual electric currents generated by these two major cortical neurons is lacking. Here, we made use of a method for vCSD analysis

(Goto et al. 2011) to evaluate the main characteristics of the current sources generated by single cortical neurons in two different situations: *1*) during spiking and *2*) when experiencing synchronized postsynaptic potentials.

Figure 2*A*, *top left*, shows the grand average of SRPs obtained for 10 putative layer IV PCs. The corresponding time courses of the monopolar, dipolar, and quadrupolar components estimated from these SRPs, and associated with backpropagating spikes along the PCs, are shown at *bottom left*. Note that at the time of maximum dipolar component (i.e., brown dashed vertical line), this type of cell shows a bipolar current source configuration (Fig. 2*A*, *top right*), as expected with a preferential orientation perpendicular to the cortical surface (Fig. 2*A*, *bottom right*). To our knowledge, this study provides the first quantitative evaluation of the maximal dipolar current generated by spiking PCs (z-direction, 49.7 ± 22.0 nA·mm; t-test significant, $P < 0.01$). Surprisingly, we found also a monopolar ($-11.7 ± 3.4$ nA; Fig. 2*C*) component that was significant at the negative peak of the spike (Fig. 2*A*, black arrow). Even though nonbalanced redistributions of the electric charge exist at each time instant, the net charge at a large temporal scale (i.e., 4 ms) was zero (Fig. 2*A*, green dashed line). Finally, the quadrupolar component produced by backpropagating spikes in this type of neuron was also significant ($51.2 ± 39.1$ nA·mm^2; t-test significant, $P < 0.05$). Therefore, in this study we confirmed experimentally a previous theoretical result by Milstein and Koch (2008) about the need for including dipolar and quadrupolar components when modeling the mesoscopic scale ($r < 1$ cm), with the difference that we have provided additional evidence for a substantial role of the monopolar term. The grand average of SRPs obtained for 10 putative SS cells as well as the respective statistics for the multipolar components are shown in Fig. 2*B*, *left*. As assumed in many previous studies, SS cells have a very symmetric current source configuration (Fig. 2*B*, *top right*), resulting in neither significant dipolar (Fig. 2*B*, *bottom right*) nor quadrupolar components at the time instant of maximal activation (brown dashed vertical line). Although it was apparently different from zero, the monopolar component at the peak of the spike (Fig. 2*B*, black arrow) was not statistically significant (i.e., $-6.7 ± 0.7$ nA; Fig. 2*C*) and, as for the PCs, the net charge at the large temporal scale was also zero (Fig. 2*B*, green dashed line).

Event-related LFPs reflect concurrent electric activity in the dendrites of large PCs over an extended cortical area. Hence, we used them to evaluate whether or not multipolar components, similar to those previously observed for backpropagating spikes along PC dendrites, also appear when many of these PCs receive synchronized synaptic inputs. First, we estimated the volume current sources s for both single and whole whisker stimulation paradigms by applying vCSD to the corresponding event-related LFPs. With the use of the DiI histological images, we were able to coregister for each single condition the image of the estimated s and that of the anatomic barrels (Fig. 3, *top right*). From visual inspection, we confirmed that the probe always covered about nine barrels. To determine the multipolar moments generated by each independent barrel, we used a single whisker stimulation protocol. For each deflected whisker, we applied a spike-sorting method to identify the most active barrel and determined its anatomic border from tangential sections of the brain with the cytochrome c oxidase immuno-
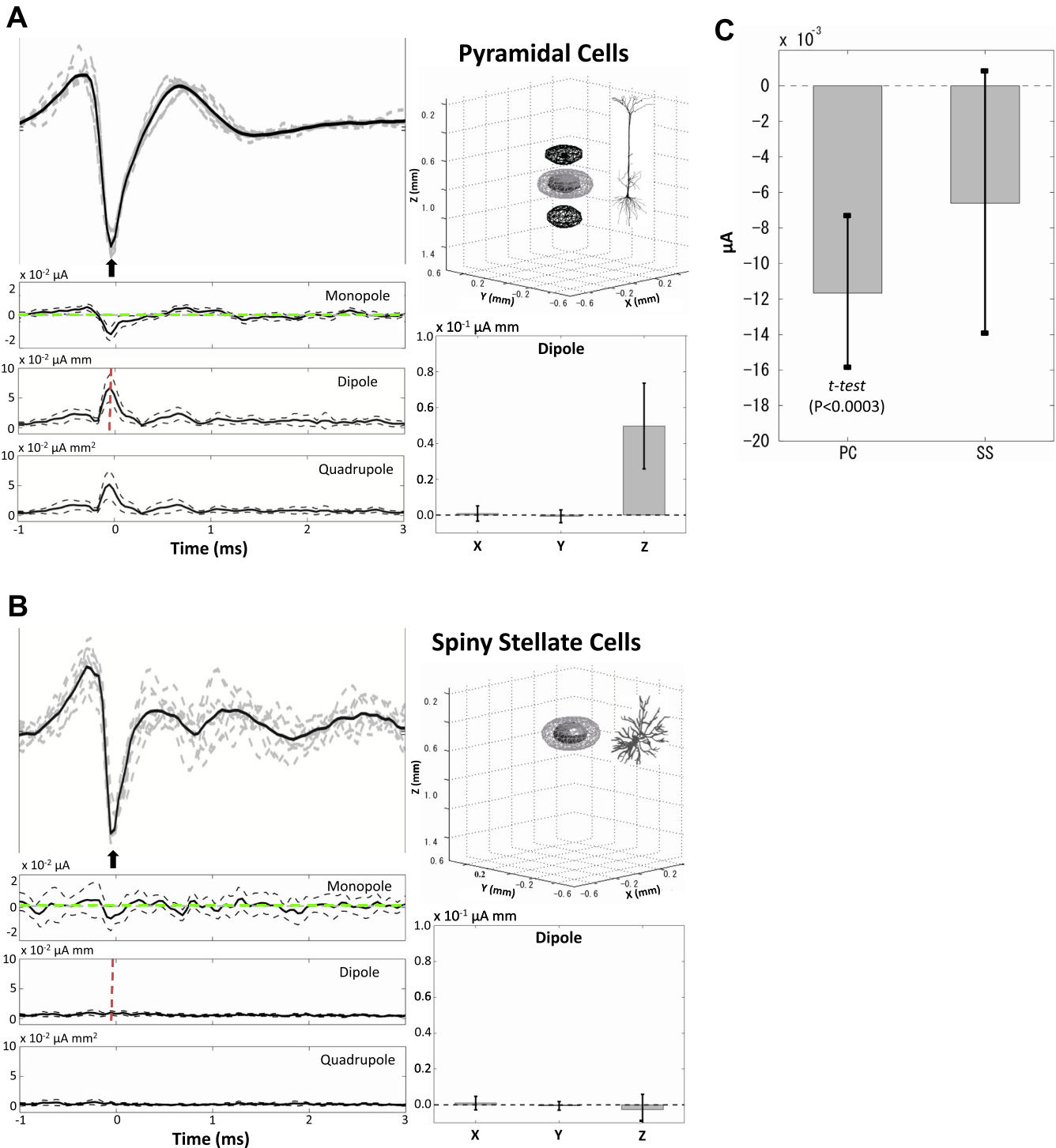
Fig. 2. Multipolar current sources for unit activity of principal cortical neurons. *A*: overlapping of action potentials generated by 10 layer V tufted pyramidal cells (PCs; gray dashed lines) is shown at *top left*. The mean of the action potentials is highlighted (black continuous line). *Top right*: spatial distribution of the volumetric current source density (CSD) generated by this cell type at the time instant of largest negativity in their action potentials (i.e., black arrow), which clearly shows a bipolar shape. The CSD distributions are represented in 3-dimensional contours. The contours denoted by meshes and patches represent the weak (30% of the maximum) and strong (70% of the maximum) intensity of the CSD, respectively. Time courses of the monopolar, dipolar, and quadrupolar moments are shown at *bottom left*. The sum of the monopolar moment along the entire time window (i.e., 4 ms) was zero (green dashed line). For the dipolar and quadrupolar moments, we calculated at each time instant the norm of the corresponding vector and tensor (i.e., the trace), respectively. The multipolar moments were calculated with respect to the center of gravity of the layer V tufted PCs. For these time series to be comparable, the multipolar moments must be standardized, taking into account the actual length of this type of PC. The dipolar moments generated by these PCs along the *x*, *y*, and *z* directions at the time instant of maximal dipolar activity (i.e., brown dashed vertical line) are revealed in the graph at *bottom right* together with their respective standard deviations. *B*: same conventions as in *A*, but for layer IV spiny stellate (SS) cells (10 cells). *C*: comparison between intensity of the monopolar moment for layer V tufted PC and layer IV SS cells at the time instant of largest negativity in their respective action potentials, i.e., black arrows in *A* and *B*, respectively.
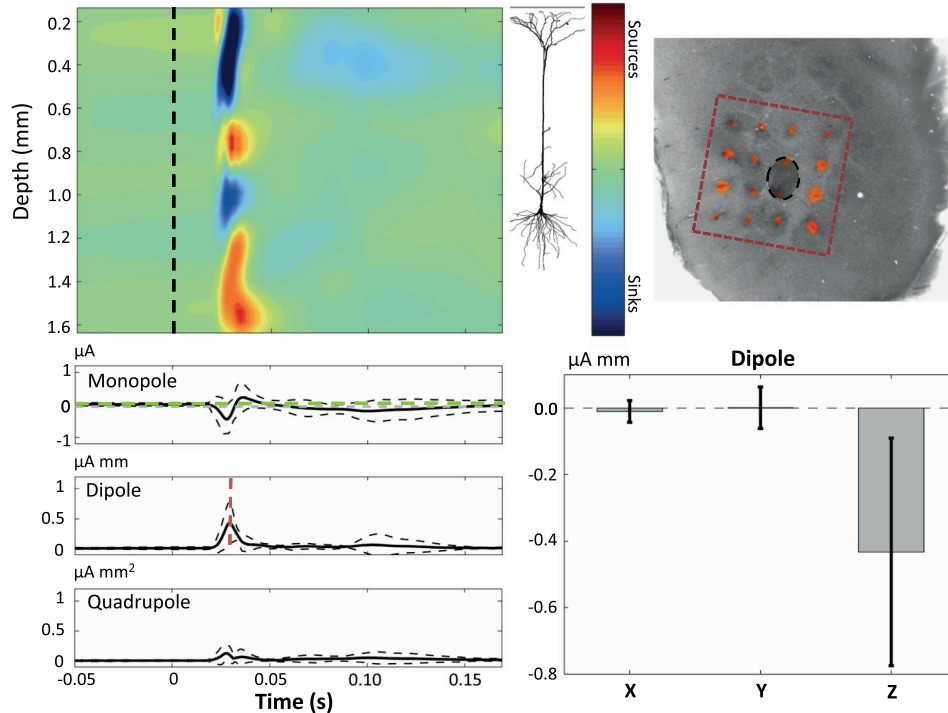
Fig. 3. A volumetric CSD analysis from LFP recorded during single whisker deflections. *Top left*: grand-average CSD spatiotemporal map obtained from averaging the *x-y* projections of the volume current sources *s* over all rats. These projections were obtained by pooling *s* along the *x-y* directions within each particular activated barrel. Black dashed vertical line indicates the time instant for the whisker deflections. The relative positions of the layer V tufted PC are presented. *Top right*: combined cytochrome *c* oxidase and DiI histological images (a tangential section) showing the position of the 3-dimensional probe with respect to the barrel field. A particular barrel is highlighted. *Bottom left*: means and standard deviations of the multipolar moments. For each deflected whisker, the corresponding multipolar moments were calculated using *Eq. 1a* with the volume of interest defined as the actual anatomic barrel. For these magnitudes to be comparable, the dipolar and quadrupolar components must be divided by l and l^2, respectively. In the case of the dipolar and quadrupolar current components, their respective norms were used. The cortical thickness l in the barrel cortex was 2 mm. As in Fig. 2, *A* and *B*, the sum of the monopolar moment along the entire time window (i.e., 200 ms) was zero (green dashed line). *Bottom right*: the dipolar components along the *x*, *y*, and *z* directions at the time instant of maximal dipolar activity (i.e., brown dashed vertical line) are shown together with their respective standard deviations.

staining. The anatomic barrel of the corresponding deflected whisker was used as the volume of interest V in *Eq. 1a* to calculate the multipolar moments associated with the barrel-wise postsynaptic evoked activity. A grand-average CSD spatiotemporal map was obtained by pooling the volume current sources *s* along the *x-y* directions within each particular activated barrel and then summing the resulting maps for all rats (Fig. 3, *top left*). Barrels that were in the border of the region covered by the 3-D probe were not included in the statistical analysis. The mean and SD of the multipolar moments obtained from single deflected whiskers for all rats are shown in Fig. 3, *bottom right*. As expected, a dipolar component at the maximal postsynaptic activity (-0.43 ± 0.16 μA·mm; *t*-test significant, $P < 0.01$) was predominantly tangential to the cortical surface. Significant monopolar (-0.44 ± 0.20 μA; *t*-test significant, $P < 0.01$) and quadrupolar components (0.13 ± 0.06 μA·mm^2; *t*-test significant, $P < 0.01$) associated with synchronized postsynaptic activity within single barrels were also observed at the time of maximal evoked response. We applied a whole whisker stimulation protocol to evaluate whether or not temporal unbalances in the charge redistributions would remain observable for volumes covering a larger cortical surface. Toward that end, we used the whole cortical region defined by our 3-D probe (i.e., 2.5-m^3 voxel) as the volume of interest in *Eq. 1*, which represents the most elemental volume in modern EEG imaging methods. For each rat, we were able to observe about four functional barrels (Supplemen-

tal Video 3). At the time instant of maximal evoked neuronal activity, we found significant monopolar components within the mesoscopic voxels (-3.32 ± 1.20 μA; *t*-test significant, $P < 0.05$) (Fig. 4). In both cases described above, the net charge at a large temporal scale (i.e., 200 ms) was approximately zero (Figs. 3 and 4, green dashed lines).

Concurrent LFP and EEG recordings. In a second experiment, we used concurrent recordings of high-resolution skull EEG and laminar LFPs to evaluate the relationship between intracortical multipolar moments and the EEG equivalent dipoles for the Wistar rat's head. To improve the signal-to-noise ratio for the EEG recordings, we used a whole whisker stimulation protocol in this experiment. Intracranial electrical re-
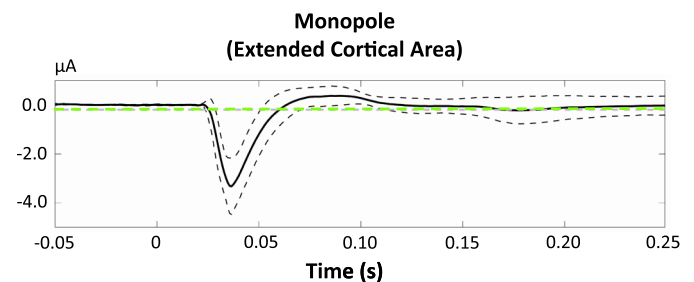
Fig. 4. Mean and standard deviation of the monopolar moment generated by a 2.5-m^3 voxel during a whole whisker stimulation protocol are shown. The sum of the monopolar moment along the entire time window (i.e., 300 ms) was zero (green dashed line).

cordings were obtained at different depths from the pial surface using both short and long probes, covering the entire cortical lamina with data from different rats. To coregister data from all experiments, we utilized cytochrome *c* oxidase, Nissl bodies, and DiI neurotracer staining images from the postmortem fixed brain sections (Fig. 5A, *left*). The relative position of the shank with respect to the barrels (areas enclosed by boxes) and septums (interspaces indicated by arrows) was estimated from the cytochrome *c* oxidase immunostaining, as was clearly

defined at the level of layer IV, and the DiI fluorescent images. For all experiments, the probe (red trace, DiI) was roughly perpendicular to the cerebral cortex and remained within a single column (i.e., a barrel) along all cortical layers. Hence, we assumed that the recorded LFP for the most part reflected neuronal activity mainly from a single barrel. Layer distributions were determined through the Nissl staining as indicated in the combined image (Fig. 5A, *right*). The interfaces between layers V/VI were easily determined from jumps in the distri-
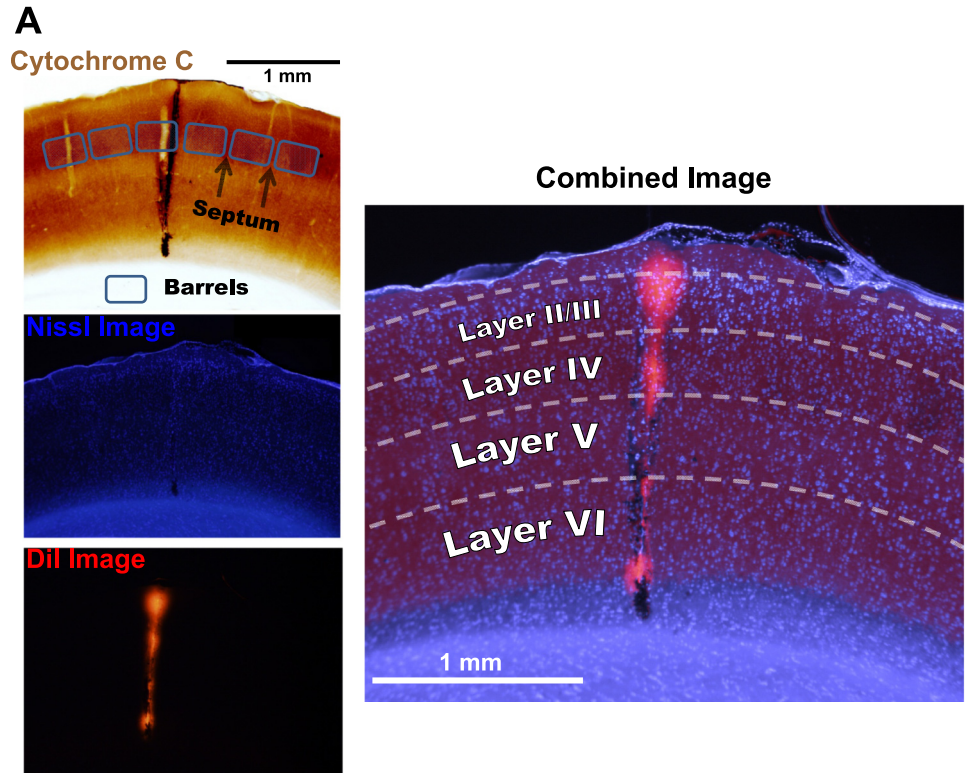
Fig. 5. *A*: histological analysis. A coronal section of the barrel cortex obtained from the postmortem fixed brain is shown. The 3 color panels (*left*) represent the cytochrome *c* oxidase (brown), the Nissl body staining (cyan), and the trace produced by the shank after the insertion (red-orange). The cytochrome *c* oxidase immunostaining helps us to determine accurately the limits of layer IV, where barrels (cyan boxes) and septums (interspaces) were clearly defined. To produce such a trace, a florescent lipophilic neuronal tracer was gently applied to the side of the probe. A long probe was used in this particular example. The cortical layer can be distinguished from the fluorescent Nissl images. Large PCs are mostly distributed around layers V and VI. The multicolor composed image is shown (*right*) with a particular distinction to the laminar profile. *B*: single-trial CSD analysis. *Top*: color maps represent the spatial distributions of LFPs in a section of the barrel cortex (0.5–1.1 mm) of a particular rat (*left*, 1 Hz; *right*, 3 Hz). The actual amplitudes (mV) of the LFPs are represented by bar color coding. The relative position of the layer V tufted PC with respect to these maps is also illustrated. *Bottom*: CSD analyses, performed with the inverse CSD (iCSD) method (Pettersen et al. 2006), from the respective LFP (*top*) are shown (*left*, 1 Hz; *right*, 3 Hz). Even for this particular trial, data were not acquired for the very superficial layers (e.g., layer I); the iCSD method provided interpolated estimators of the volume current sources in these layers under boundary condition $s(z)_{z=1} = 0$ on the pial surface.
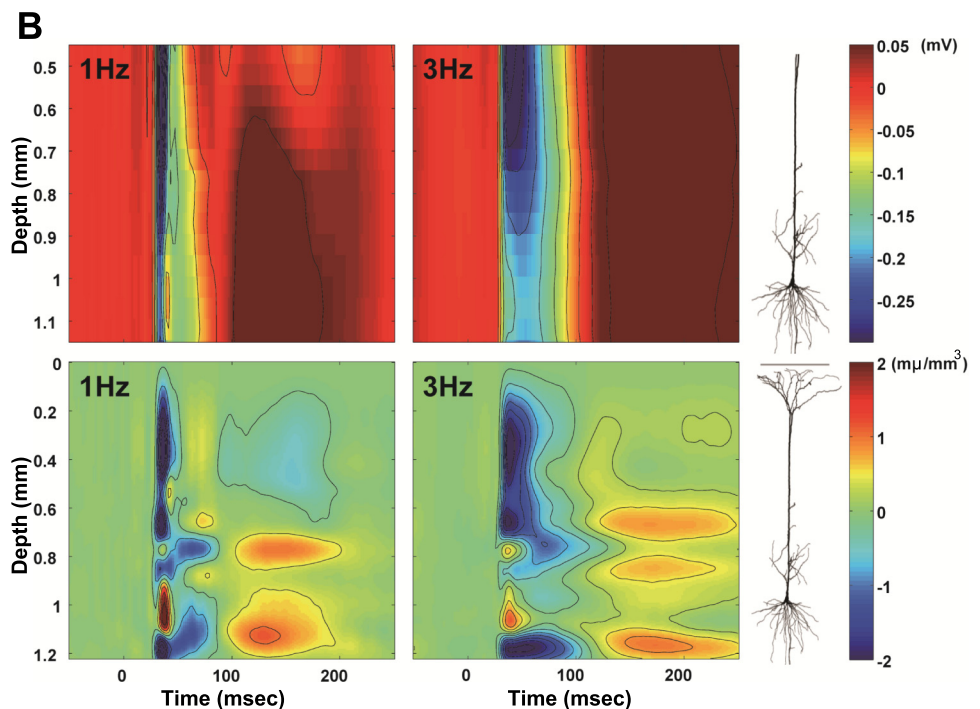
butions of the large PCs. The limits of layer IV were evident from the intensity of the immunoreactions to cytochrome *c* oxidase. Layer I was characterized by a low density of Nissl bodies. In each recording, the microelectrodes in the probe covered a region of about either 800 or 1,600 μm in length for the short and long probes, respectively. A typical example of the event-related LFP recorded with a short probe is shown in Fig. 5*B*, *top*. In this case, the spatiotemporal pattern is consistent with LFP observations from a region between layers II/III (middle) and V. Figure 5*B*, *bottom*, shows the corresponding CSD analysis for these particular LFP data. By imposing a zero boundary condition on the volume current sources at the pial surface and at the interface with the gray matter, the iCSD method is able to estimate the current sources from deeper layers up to the most superficial layers. A small standard deviation was observed from the inter-rat CSD statistical analysis, which indicates a reproducibility of the CSD maps for the entire barrel cortex (data not shown).

After coregistration, we were able to create, from all trials and rats, a grand-average color map of the event-related CSD of the entire barrel cortex (Fig. 6, *top*). At each time instant, we

estimated the center of charge z_c as that cortical depth for which positive and negative net charges were equally distributed on both sides:

$$z_c(t) = \min_{z_m} \int_0^l s(z,t) \left| z_m - z \right| dz \qquad (7)$$

We found that the center of the charge in the neocortex fluctuated very rapidly with time, although it seemed quite stable shortly after the stimulus onset. The CSD spatiotemporal patterns were very similar to those reported in a previous work (Di et al. 1990; Barth D, personal communication, Fig. 3). In our experiment, 1-Hz stimulus frequency constitutes the closest condition to that used in this previous study. For that particular condition, the main common characteristics between our CSD pattern and that found by Di et al. (1990) were *1*) an early sink in layers II/III–IV with a very short duration; *2*) at the level of layer IV, this sink was followed by a long-lasting weak source; *3*) the peak amplitude of such a source component delayed and intensified while approaching layer V; *4*) there was a rapid change of polarity in layer V soon after the stimulus onset; and *5*) a short source at layer VI was followed
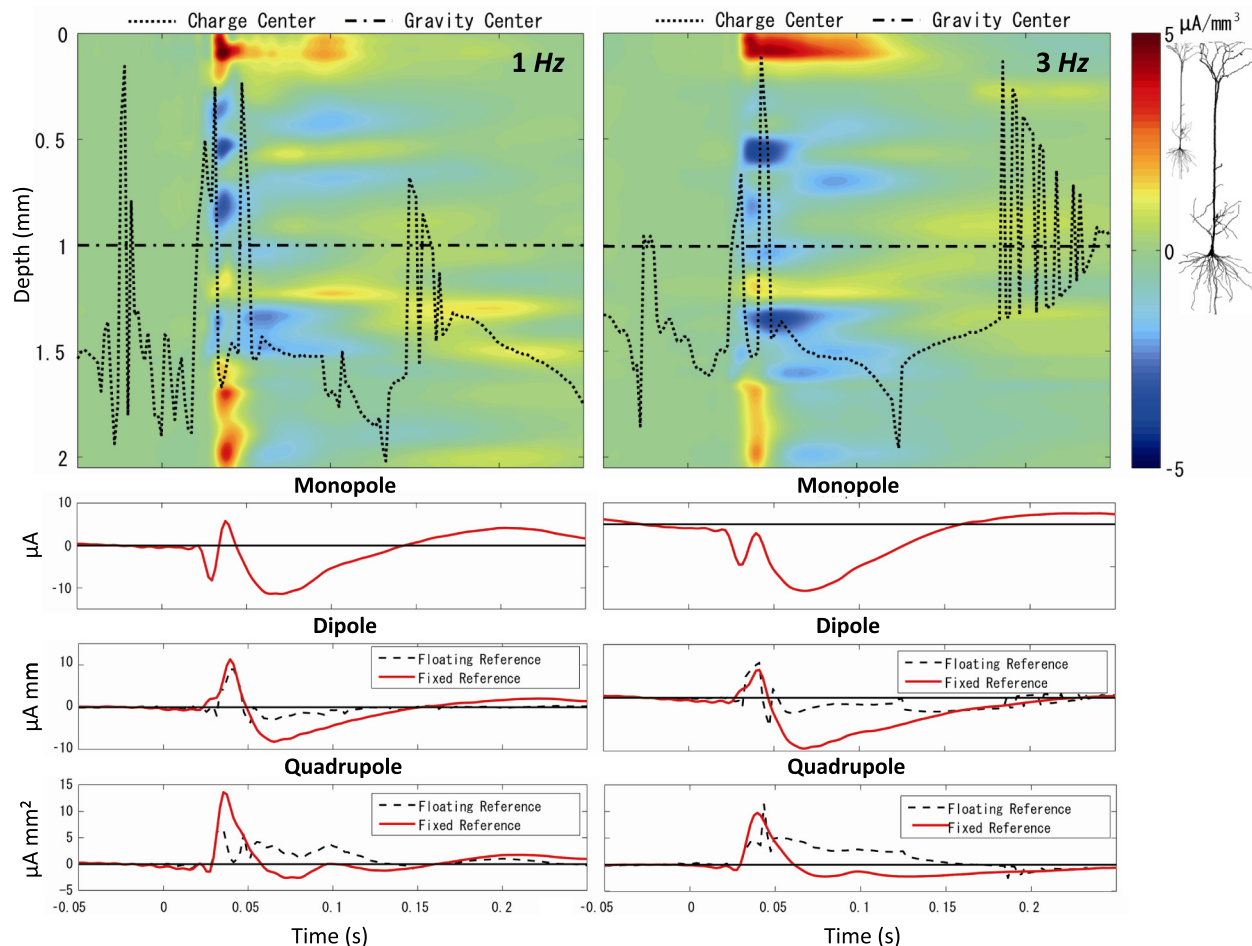
Fig. 6. Population CSD analysis. *Top*: the means of the CSD single trials (all experimental data) calculated using the iCSD method are shown (*left*, 1 Hz; *right*, 3 Hz). These means were calculated after the probes used in all experiments were coregistered by means of the immunostaining images. The insertion depths of the probes were different from trial to trial and were defined in that way to cover the whole *z*-axis of the barrel fields. In some cortical layers, the sink/source arrangements showed dipolar-like symmetries, but in others, more complex spatiotemporal patterns were obvious. The relative positions of the layer II/III PC and layer V tufted PC are also exposed. To quantify the charge balance along cortical layers, the multipolar moments (*Eq. 1b*) were calculated from the mean CSD. *Bottom*: time courses of the monopolar, dipolar, and quadrupolar moments are shown. The multipolar moments were calculated with respect to the center of gravity of the cerebral cortex (i.e., 1-mm depth). Use of the center of the charge produced time courses with no clear meanings. For comparison, these moments must be standardized, taking into account the actual cortical thickness.

by a nonpronounced but longer sink. In our case, there was also an early source in layer I, but it was not followed by an extended sink as in that previous work. Similar CSD spatio-temporal patterns for the earliest time window (up to 50 ms after the stimulus onset) have been reproduced in more recent studies (Higley and Contreras 2007; Mégevand et al. 2008). Note that in these last two studies, the colors yellow/red and blue are used for sinks and sources, respectively. We also observed symmetrical source arrangements (i.e., sink/source/sink patterns) around layer IV, which are distinguished in Mégevand et al. (2008, Fig. 2). Such a CSD profile may be associated with the early activation of spiny stellate cells, the main target of thalamocortical axon terminals. The time courses of the current sources presented in this study seem to be shifted 15 ms with respect to those observed in previous studies. We employed a 2-m silicon tube from the high-pressure air tank to the needle's tip, which introduced an undesirable delay in the deflections of the whiskers. In the abovementioned previous studies, electromechanical devices (i.e., piezoelectric stimulators) were used. Furthermore, in our experimental paradigm, all left whiskers were simultaneously deflected, whereas in two of the previous studies, selective whiskers were stimulated (Di et al. 1990; Higley and Contreras 2007).

We calculated the multipolar moments by using *Eqs. 1b*. The time courses of the multipolar moments with respect to the center of gravity of the cortical column are shown in Fig. 6, *bottom* (red continuous line). Also shown are the time courses when the center of charge was used instead (black dashed lines), which produced dipolar and quadrupolar moments with questionable waveforms. In agreement with our first findings, there were robust contributions from the monopolar and quadrupolar components to the mesoscopic volume current sources in the barrel cortex. The maxima amplitude of the monopolar and dipolar currents, generated by a single barrel, was approximately the same, whereas it was relatively smaller for the quadrupolar current. Despite the similarities in the time courses of the multipolar moments in Figs. 3 and 6, they differ in some features. Differences in the stimulation protocols (i.e., single vs. whole whisker), the probe formats (i.e., laminar vs. three-dimensional), and the source model (i.e., cylindrical symmetry/interpolation and smoothing) might underlie such discrepancies.

The event-related EEG signals at all electrodes for 1 and 3 Hz are shown in Fig. 7*A*, *top*, which reveals the presence of four main components along the time course (C1–C4, marked with vertical blue lines). The topographic color maps of each component (plotted on the rat's actual skull) are shown in the respective *bottom* panels for both stimulus frequencies. The expected contralateral components were not only in the primary and secondary somatosensory cortices but also in a large portion of the motor cortex, as can clearly be identified from these topographic maps (Boorman et al. 2010; Mégevand et al. 2008; Petersen 2007). Ipsilateral activation of the primary somatosensory cortex is also exposed. The spatiotemporal event-related EEG topographic maps for a particular rat are shown in Supplemental Videos 4 (conditions: *A*, 1 Hz; *B*, 3 Hz). Similar topographic patterns in space and time were found in all rats. To quantify the reproducibility among rats, we estimated not only the event-related

EEG signals but also the standard deviations for all electrodes and stimulus frequencies. As shown in Fig. 7*B* for *electrode 14*, the signal-to-noise ratio was adequate and the EEG data were very reproducible.

In this study, we estimated two particular types of EEG inverse solutions (i.e., least-squares dipolar fitting and surface LORETA, Table 1) from the skull EEG data. First, we estimated the time-varying amplitude of an equivalent current dipole using a least-squares fitting strategy (Jones et al. 2007). This equivalent current dipole was placed in the center of the barrel field for each rat, which was determined by semiautomatically coregistering the T1-weighted anatomic images with a digitalized atlas of the Wistar rats (Paxinos and Watson 2007). The direction of this equivalent current dipole was set perpendicular to the cortical surface and positioned at a depth of 1 mm. Following the methodology suggested by Jones et al. (2007), we estimated the additional free moving equivalent current dipoles until the goodness of fit was larger than 75%. We used the χ^2 criterion for the goodness of fit, assuming that the EEG data probability density function was Gaussian. The effect of these free moving dipoles was removed from the data using the signal-space projection method. The final waveform of the equivalent current dipole in the barrel field was refitted to the residual (Fig. 8, *top*). Second, the surface LORETA was implemented using the discrete Laplace-Beltrami operator for the cortical surface as the regularizing matrix (Riera et al. 2000). To avoid singularities in the regularizing matrix due to the harmonic subspace (i.e., the constant functions), we disconnected the vertexes of the left and right hemispheres, which was equivalent to introducing a boundary condition at the level of the corpus callosum. The topographic maps on the cortex obtained from the surface LORETA were not in disagreement (data not shown) with previous findings obtained using other neuroimaging techniques (voltage-sensitive dyes: Ferezou et al. 2007; functional MRI: de Celis Alonso et al. 2008). We pooled the amplitudes of the surface LORETA inverse solution for vertexes in close proximity to the center of the barrel field, which allowed us to have a time series for each rat equivalent to that obtained from the least-squares dipolar fitting (Fig. 8, *bottom*).

The final result of the source analysis is a waveform $d_{IS}^F(t)$ for each inverse solution type (*IS*) and stimulus frequency (*F*). To evaluate the impact of multipolar components on large-scale observations, we performed a linear regression analysis (*Eq. 8*) for each rat. In this analysis, which was motivated by the particular dependency of the multipolar moments (i.e., m_z, d_z, and Q_z) in *Eq. 4*, the time courses of the normalized multipolar moments obtained from the small-scale LFP data through *Eqs. 1* (Fig. 6, *bottom*) were used as known linear regressors ("loadings") of the waveforms $d_{IS}^F(t)$.

$$d_{IS}^F(t) = \chi_c^{\{IS,F\}} + \chi_m^{\{IS,F\}}m_z(t) + \chi_d^{\{IS,F\}}d_z(t) + \chi_Q^{\{IS,F\}}Q_z(t) \tag{8}$$

The coefficient $\chi_c^{IS,F}$ was introduced to account for any difference in the baseline. Figure 9 illustrates the result of such a linear regression from a particular rat for both dipole-fitting (*top* panels) and LORETA types of inverse solution (*bottom* panels). The respective estimated coefficients $\chi_L^{IS,F}$, L = {*c, m,*

A
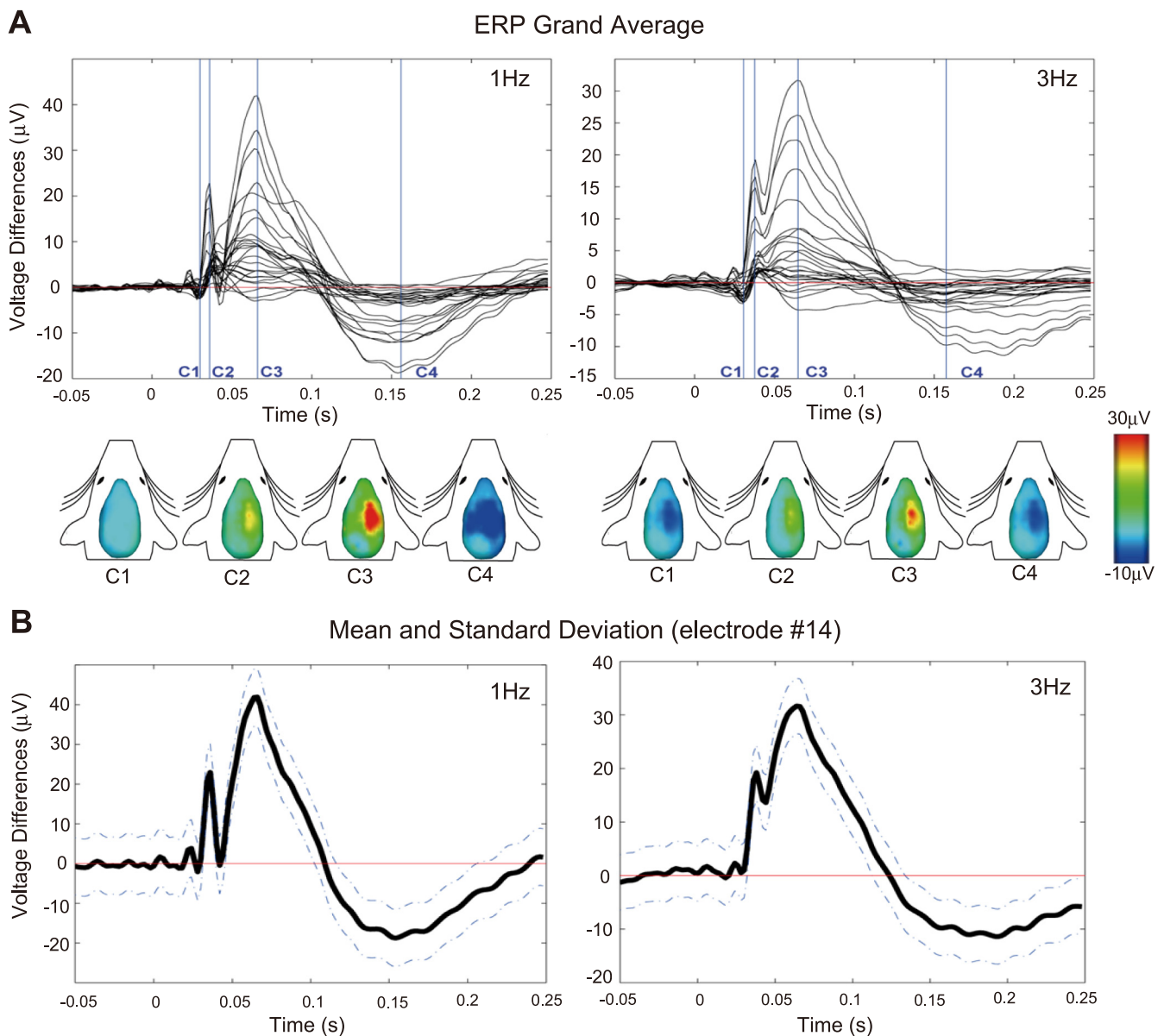
Fig. 7. Event-related EEG signal. *A*: event-related EEG signals are shown at *top* for both stimulus conditions (*left*, 1 Hz; *right*, 3 Hz). Four main components (C1–C4) were clearly distinguished, which are probably related to the activation of the primary somatosensory/motor cortices. Their corresponding topographic maps on the skull, shown at *bottom*, reveal their much extended spatial patterns. The time instants for these components are marked with vertical lines. *B*: time course of the event-related EEG signal, with the respective standard deviation, for 1 particular electrode (*electrode 14*, close to the barrel cortex) is shown. The interindividual variability was small compared with the size of the event-related response.

$\vec{\mathbf{d}}$, $\overleftrightarrow{Q}$ }, obtained from all rats for both types of inverse solutions and stimulation frequencies are shown in Fig. 10. To compare the contributions of these multipolar moments to the large-scale waveforms $d_{IS}^F(t)$, we performed a two-way ANOVA with multiple comparisons. The current monopoles were the most significant source component of the $d_{IS}^F(t)$ waveforms. The current monopoles were relatively larger for the 3-Hz stimulation condition, whereas quadrupolar contributions were larger for the 1-Hz stimulation condition. The equivalent current monopolar and quadrupolar components have opposite signs for both stimulation conditions. These characteristics were very well captured by both types of inverse solutions. The dipolar components were positive for the 1-Hz stimulation condition but revealed a change in polarity between dipole-fitting

and LORETA inverse solutions for the 3-Hz stimulation condition. The estimated macroscopic dipoles in the barrel cortex revealed a dynamic content that resembles mesoscopic monopolar components more prominent for the surface LORETA inverse solution than for the dipole-fitting inverse solution. The goodness of fit for each inverse solution is summarized in Table 2. As expected, the surface LORETA inverse solution always provided the best goodness of fit. Finally, we evaluated the contribution of each multipolar regressor to the large-scale waveforms $d_{IS}^F(t)$ by combining the same linear regression analysis with a "leave-one-out" strategy. In the leave-one-out strategy, we performed a linear regression analysis with only two multipolar regressors, leaving one of them (e.g., monopole, dipole, or quadrupole) out of the linear model (8).

Table 1. *Main characteristics of two inverse solutions used to evaluate the impact of multipolar current sources on EEG data*

Inverse Solution	Source Model	Constraints
Equivalent dipole	Dipole	Orientation/location "fixed"
LORETA	Dipole	Spatial smoothing

The estimation errors (Table 2) clearly revealed a major contribution to $d_{IS}^F(t)$ of the monopolar current sources.

DISCUSSION

On the basis of recent advances in both techniques for electrophysiological recording and methodologies for CSD analysis, we have revised in this study significant biophysical aspects of the genesis of extracellular potentials. Keeping in agreement with previous experimental data, we observed that cortical PCs are the cells that contribute the most to both the small-scale LFP and large-scale EEG data. However, for the first time, quantitative values of the actual electric currents produced by PCs, either while spiking or during the integration of synchronized postsynaptic potentials, are provided. As suggested theoretically in the past (Milstein and Koch 2008), we found that not only dipolar but also quadrupolar components emerge in the LFP up to distances of almost 1 cm. More importantly, we have presented evidence for a remarkable unbalance in the instantaneous charge redistribution during different types of neuronal activation, at least for the sampling rate normally used to observe electrophysiological signals. With a basis on linear regression analysis, we examined the

similarities between the dynamics of each multipolar component reconstructed using intracranial laminar LFP from the barrel cortex and that of an equivalent dipole estimated from the skull EEG data. Unexpectedly, the time series of the equivalent EEG dipole were much better represented by the intracortical monopolar loadings than by the dipolar ones. Signs of the intracortical quadrupolar components were found in the skull EEG, but by some undetermined reasons, the regression coefficients were consistently negative. In the particular case of Wistar rats, the electrodes are positioned very close to the cortical current sources (~1 cm), a fact that may underlie the existence of quadrupolar components for EEG data in this study. These last results indicate that any EEG inverse solution based on a dipolar model will comprise not only the mesoscopic dipolar components but also those monopolar and quadrupolar components. Our conclusions are founded on data recorded from the barrel cortex of Wistar rats, a cortical region that has been very well studied in the past. Regardless of several particulars for the barrel field, columns in other cortical regions of mammals share many similarities with the barrels in terms of the laminar organization, cellular distribution/orientation, and microscopic circuitries. Therefore, our present conjecture is that our results about the multipolar profile of the LFP are valid for the neocortex in general. However, our conclusions about the contributions of the intracortical multipolar moments to the EEG macroscopic observations will definitely depend on the size of the head for each particular species as well as on the relative position of the EEG electrodes with respect to the cortical mesoscopic patch of interest.

Fig. 8. EEG inverse solution in the barrel field. The mean amplitudes of the equivalent current dipole $d(\vec{r}, t)$ [i.e., $d_{IS}^F(t)$] for the barrel field are shown for both stimulus frequencies. This magnitude was estimated using the single dipole-fitting strategy (*top*) and the surface LORETA inverse solution (*bottom*). The standard deviations are represented by dashed lines. The estimated dipole amplitudes revealed very consistent waveforms across all experiments.

Single Dipole vs. Multipole Expansion
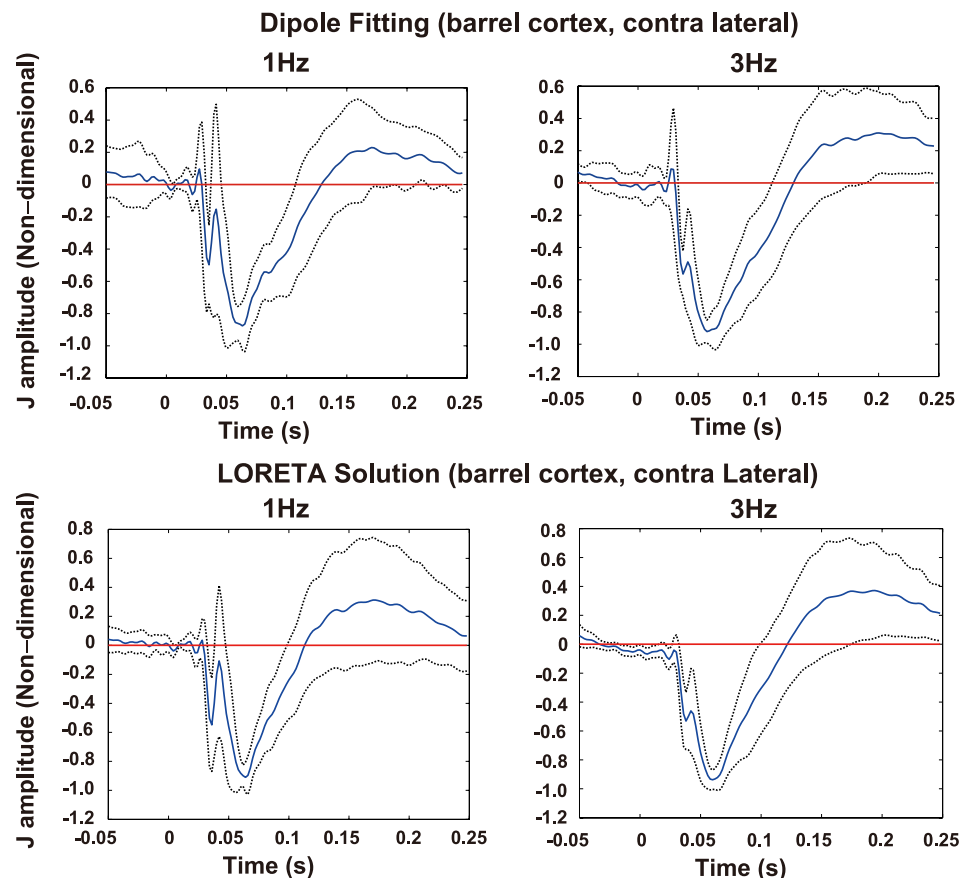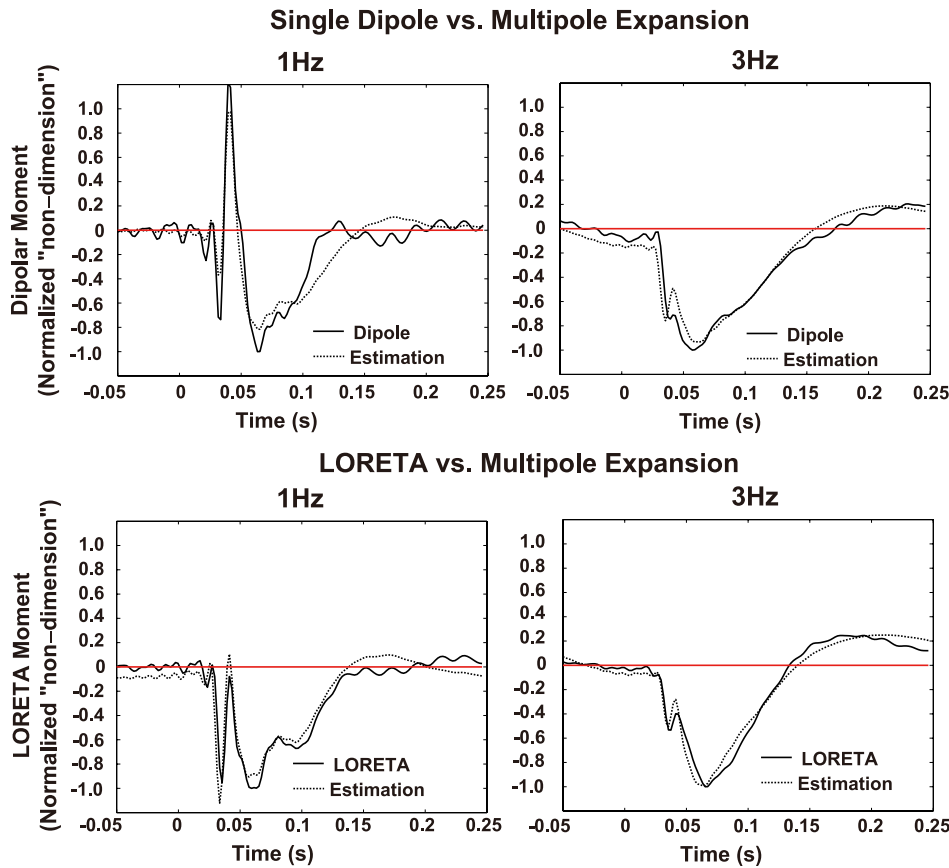
Fig. 9. Linear regression analysis. Comparisons of the actual large-scale waveform $d^F_{IS}(t)$ (black line) resulting from each inverse solution and that reconstructed by the linear regression model (black dotted line) are shown for dipole fitting (*top*) and LORETA inverse solution (*bottom*). *Left* and *right* panels show results for 1- and 3-Hz stimulation frequencies, respectively. The large-scale waveforms $d^F_{IS}(t)$ were normalized to the minimum peak at 60 ms after stimulus onset, a characteristic that was very replicable for all inverse solutions and stimulation frequencies.

Plausible scenarios for a mesoscopic CSD unbalance. The existence of unbalanced current sources in the neocortex constitutes one of the most provocative findings of this study. The introduction of monopole current source models to describe

Fig. 10. Statistical comparison of the multipolar components. The contribution of monopole, dipole, and quadrupole to large-scale waveforms $d^F_{IS}(t)$ are shown for different inverse solutions and stimulus conditions. Values of the linear regression coefficients $\chi^{IS,F}_L$ are presented in a bar-plot style with the respective standard deviations estimated using data from the 9 rats. Coefficients for the monopolar components were significantly larger than those for the dipolar and quadrupolar components (2-way ANOVA with multiple comparison, $P < 0.0001$).

EEG data might raise questions about whether or not any well-established laws of physics are violated. Here, we propose two scenarios to rationalize this result without having to assume that electrical charge is either created or destroyed. First, note that, at any location, the temporal average of the monopole current source was zero, and consequently, no charge accumulates anywhere over time. The CSD unbalance is then an issue related to the relative timescales for both the charge movements and the observed EEG signals. To solve the EEG forward problem, we generally assume that the total electric current $\vec{J}_{Total}(\vec{r},\,t)$ inside any mesoscopic area in the brain is defined as a superposition of nondispersive ohmic

Table 2. *Goodness of fit for each inverse solution and estimation errors in the linear regression analysis*

		Linear Regression Analysis			
				Leave One Out	
Stimulus Frequency	Goodness of Fit, %	Three Multipoles	Monopole	Dipole	Quadrupole
Equivalent dipole					
1 Hz	61	0.17 ± 0.08	0.23 ± 0.07	0.19 ± 0.08	0.20 ± 0.08
3 Hz	75	0.11 ± 0.08	0.17 ± 0.09	0.13 ± 0.08	0.13 ± 0.07
LORETA					
1 Hz	65	0.17 ± 0.06	0.25 ± 0.10	0.19 ± 0.05	0.20 ± 0.05
3 Hz	83	0.11 ± 0.07	0.19 ± 0.10	0.13 ± 0.08	0.13 ± 0.06

Estimation errors in the linear regression analysis are separated into those resulting from use of the 3 multipolar regressors and those obtained using a leave-one-out strategy by which the monopolar, dipolar, or quadrupolar regressor (as indicated) was excluded from the linear regression model.

electric currents $\vec{\mathbf{J}}_{Ohm}(\vec{r}, t) = \overset{\leftrightarrow}{\sigma}(\vec{r})\vec{\mathbf{E}}(\vec{r}, t)$ and of certain "impressed" current sources $\vec{\mathbf{J}}_p(\vec{r}, t)$. The magnitude $\vec{\mathbf{E}}(\vec{r}, t)$ represents the electric field, and $\overset{\leftrightarrow}{\sigma}(\vec{r})$ is the conductivity tensor of the brain tissues. Hence, it is believed that any charge movement in the brain tissue is only caused by the action of an electric field. Under the validity of the quasi-static approach for the electromagnetic field, the EEG forward problem is then formulated as the solution of the principle of current conservation $\nabla \cdot \vec{\mathbf{J}}_{Total}(\vec{r}, t) = 0$.

First scenario: the spatial dependency of the tissues polarization. It has been shown that, as a consequence of two major dielectric relaxation mechanisms (i.e., the counterion and interfacial polarizations), the brain tissues are highly dispersive for the frequency range of the electrophysiological recordings (Gabriel et al. 1996, 2009). In addition, the conductivity and permittivity depend on the location (i.e., inhomogeneity) and direction (i.e., anisotropy) inside the brain (Gabriel et al. 2009; Goto et al. 2010). Therefore, as charge moves, its effect on externally measured fields can depend on location. Also, at the spatial scale of single cells, the charge moving in the cytoplasm caused by a neuronal event will be detected with longer delays than that moving along the interstitial space. Thus, in the timescale of EEG observations, it is perfectly reasonable for a current sink to appear temporarily as charge enters the cell, to be replaced by a current source at a slightly later time as the charge leaves the cell. At the level of a mesoscopic volume (e.g., a barrel), brain tissues may additionally behave like a multiple spatial filtering device with frequency characteristics depending on location/orientation. Bearing in mind that the LFPs are obtained through filters that attenuate signals with frequencies higher than a cutoff frequency (i.e., ~500 Hz), one must be careful when assuming that any local closed loop inside the tissue can be ideally modeled as an resistor-capacitor (RC) circuit. Indeed, even though the total electric current is conserved within a loop comprising two regions with different electric permittivity/conductivity profiles, the observed electric currents (i.e., limited to a particular frequency range) may look unbalanced to all appearances (see APPENDIX A).

Second scenario: charge diffusion and buffering. Chemical gradients and active transport mechanisms across cellular membranes cause also significant charge movements in the brain tissues. For example, a significant contribution of ionic diffusion currents perpendicular to the neuronal membranes inside the neocortex were recently estimated by Bédard and Destexhe (2009) and was about 100 times greater than the ohmic electric current at 100 Hz. Consequently, these authors represented any type of current source of the EEG as a superposition of a finite number of monopolar sources. Alternatively, brain cells are endowed with a variety of mechanisms to transport ions across their membranes. An example of that is the ion pumping by the Na^+-K^+ and Ca^{2+} ATPases in neurons to reestablish ion gradients after the opening of voltage/chemical-dependent channels. Another example is the glutamate recycling via the EAAT1 and EAAT2 enzyme (Riera et al. 2008), which might implicate considerable buffering of ions in the neocortex during an increase of the neuronal activity. These principal buffering systems may also contribute to a redistribution of the electric charge across the cellular membranes regardless of the principle of current conservation. However, these mechanisms operate with a very low dynamic range, and

the CSD unbalances reported in this study were in the order of a few hundred milliseconds. Hence, buffering effects may cause CSD unbalances but should not be considered as the major mechanism. A more detailed discussion about ion diffusion can be found in APPENDIX B.

Finally, we discuss possible undesirable situations that could bring about an apparent unbalance in the observed current sources. First, there exist many vessels and axons in the neocortex that could cause a shunting of electric currents to remote locations and hence bring about an apparent unbalance in the observed current sources. For example, electric current shunting by pial blood vessels has been reported in the past up to 10% (Ranck 1963). Also, it has been proven that voltage fluctuations associated with dendrosomatic synaptic activity are able to propagate long distances along the axons (Shu et al. 2006), which may involve electrotonic current leakages from somas to faraway presynaptic terminals. In this study, the reference and ground for the intracranial electric recordings were on the skull and in close proximity to the barrel cortex. Consequently, we believe any electric current shunting through the vessels was minimized by this recording protocol. To evaluate the impact on the CSD distribution of any electric current shunting through the neuronal axons, in vivo simultaneous observations of intracranial and intracellular electric potentials are required in the future.

Second, on the basis of previous results by Brankačk et al. (1993), readers may be concerned about alterations in the CSD profiles along the cortical layers for the particular case of using AC-coupled intracranial electric recordings. In particular, electrical potentials recorded with the PZ2 amplifiers (TDT) are AC-coupled through *1*) a serial input capacitor (4.7 μF) connected in parallel with a grounded resistance of 100 kΩ and *2*) a serial output capacitor (0.1 μF). Trivially, given that the CSD analysis results from applying a linear operator on the observed electric potentials at each time instant, a common AC coupling to all electrodes will cause no alteration in the instantaneous CSD charge balance. Furthermore, we verified that event-related LFP associated with single whisker deflections showed typical waveforms for all shanks in the silicon-based probes. Hence, spatial distortions of the LFP caused by either an incomplete/unequal recovery or damage of the brain tissue were ignored. In the analysis, we did not include any experimental data containing suspicious artifacts, and we excluded those animals with bleeding and/or swelling around the cortical region of interest. Therefore, we hypothesize that it is the limitations in the time resolution to observe extracellular potentials together with either the spatial dependency of the dispersive relationships in the cortical tissues or the ion diffusion effects that actually underlie the existence of the monopolar components reported in this study.

The equivalent current dipole in the neocortex. In the past, when theoretical frameworks were constructed to simulate the genesis of EEG and MEG data, microscopic current sources had been assumed to be miniaturized intracellular dipoles acting on the external medium. In particular, Okada's group in Albuquerque studied the impact of the intrinsic ionic conductances (ligand and voltage sensitive) and the morphology of PCs on the spatiotemporal characteristics of such intracellular dipoles and hence on macroscopic observations. In a pioneering work, Murakami et al. (2002) proposed a single theoretical framework to interpret both small (intra- and extra-) cellular

potentials and MEG data recorded from hippocampal slices (0.4 mm thick, about 6 mm wide, and 2 mm high). This framework was based on calculations of intracellular microscopic dipoles from a mathematical model for PCs in the CA3 region (Traub et al. 1991). Using this framework, these authors were able to reproduce changes in the magnetic field waveforms/amplitudes on a mesoscopic scale (i.e., MEG detection coils were 2 mm from the slice) induced by a variety of pharmacological manipulations. Based on equivalent ideas, biophysical models for mesoscopic regions in the neocortex have been used latterly to explain large-scale electrophysiological data (Jones et al. 2007, 2009; Murakami and Okada 2006). Recently, Riera et al. (2006) proposed a simple way to include effective electrotonic resistive and capacitive ratios in a forward/generative EEG model based on a three-compartment representation of the layer V tufted PC. In this previous study, these authors suggested a very descriptive relationship between this biophysical model and the dipolar current sources in the visual cortex of humans (Riera et al. 2007). They hypothesized that when the stimulation frequency is increased, the returning capacitive currents across the neuron membrane will start showing a saturation phenomenon due to an existing limit for its time relaxation. This phenomenon is appreciated from a frequency of stimulation above 4 Hz. In our present study, the dipolar contributions were significantly smaller in the 3-Hz stimulation condition for the case of dipole fitting, whereas monopolar contributions were larger for both types of inverse solution. Our findings are in agreement with the hypothesis of Riera et al. (2006) due to the fact that dipolar components could also be majorly determined by the response capability of the membrane capacitors, i.e., the more saturated the membrane capacitor, the smaller the dipolar contribution could be to the extracellular potentials.

On the other hand, by comparing *Eqs. 2b* and *4*, we could erroneously judge the existence of a mathematical ambiguity. Fortunately, such is not the case given that $I(\vec{r}, t)$ and $m(\vec{r}, t)$ are magnitudes associated with different spatial scales. Inside the mesoscopic level, the volume current sources can be written in terms of a continuous vector field of electric currents $\vec{j}_m^p$, i.e., $s = -\nabla \vec{j}_m^p$ (dimensions: $\vec{j}_m^p \sim \mu A/mm^2$). However, we have to be prudent when extending this concept to the macroscopic level. For example, the definition of a mesoscopic monopolar source at $\vec{r}_0$ implies that a positive electric current is spreading out in the radial direction from that location. Therefore, a mesoscopic vector current source is not defined at $\vec{r}_0$. Nunez and Srinivansan (2006, see Appendix K) discussed some related aspects. We believe multipolar moments at $\vec{r}_0$ in a mesoscopic sense will be better defined in terms of the respective equivalent magnitudes: $m(\vec{r}, t) = m(t)\delta(\vec{r} - \vec{r}_0)$, $\vec{d}(\vec{r}, t) = \vec{d}(t)\delta(\vec{r} - \vec{r}_0)$, and $\overleftrightarrow{Q}(\vec{r}, t) = \overleftrightarrow{Q}(t)\delta(\vec{r} - \vec{r}_0)$.

Future remarks. In this study, we have found that current monopoles and quadrupoles constitute significant source components of the skull EEG in the barrel cortex of Wistar rats. Therefore, forward/generative models for EEG data observed from rodents must be generalized in the future to include multipolar current configurations for any mesoscopic region. On the basis of our results, we suggest the following strategy to solve the EEG inverse problem in rodents:

- Obtain characteristic dynamic equations of the multipolar current sources in the cortical columns from biophysical models of the principal neurons. These models must be descriptive rather than exhaustive, but must take into account ionic diffusion mechanisms as discussed above and the relevant geometrical characteristics of neurons. However, statistical magnitudes (e.g., occurrence probability of postsynaptic currents, neuronal firing rate) impacting on the states of these neuronal populations must be clearly represented.
- Estimate the mesoscopic monopolar, dipolar, and quadrupolar current sources from large-scale EEG data by solving a generalized inverse problem that makes use of both the characteristic dynamic equations and specific forward/generative models for all these types of current sources. Because of the differences in EEG and MEG observation modalities in terms of their visibility to multipolar current sources, it is recommended that this step be performed from concurrent EEG and MEG recordings.
- Estimate the microscopic volume current sources $s(\vec{r}, t)$ from the mesoscopic multipolar moments using *Eqs. 1*. Finally, reconstruct the dynamics of the above-mentioned statistical magnitudes from $s(\vec{r}, t)$ using the characteristic dynamic equations.

Finally, the existence of monopolar current sources in the neocortex of mammals would make a difference when comparing EEG and MEG data, since this type of current source would have no effect on the magnetic field. In our view, the existence of monopoles could give an alternative explanation to the large differences found in the EEG and MEG waveforms associated with interictal spike activity in a variety of epileptic patients (Fernandes et al. 2005; Huiskamp et al. 2004), a phenomenon difficult to explain with a single dipolar source under the quasi-static approach for the Maxwell equations. At this moment, alternative hypotheses for such waveform discrepancies are *1*) the spatiotemporally distributed nature of these sources (Huiskamp et al. 2004) and *2*) the differences in the orientations of the underlying dipolar source (Fernandes et al. 2005).

APPENDIX A: THE SPATIOTEMPORAL FILTERING PROPERTIES OF THE CORTICAL TISSUES

In brain tissues with multiple and noninstantaneous dielectric relaxation mechanisms, the constitutive relationships depend in a very particular way on the frequency within specific ranges. Also, as a consequence of the existence of complex microscopic structures in the brain tissues, both conductivity and permittivity could depend on location (i.e., local inhomogeneities) and orientation (i.e., local anisotropies). For example, the existence of significant ionic diffusion might indirectly affect the electric permittivity $\overleftrightarrow{\varepsilon}(\vec{r}, \omega)$ due to counterion polarizations at low frequencies ω.

$$\vec{D}(\vec{r}, t) = \int_{-\infty}^{\infty} \overleftrightarrow{\varepsilon}(\vec{r}, \tau)\vec{E}(\vec{r}, \tau)d\tau \qquad (A1a)$$

$$\vec{J}_{Ohm}(\vec{r}, t) = \int_{-\infty}^{\infty} \overleftrightarrow{\sigma}(\vec{r}, \tau)\vec{E}(\vec{r}, \tau)d\tau \qquad (A1b)$$

In other words, $\vec{J}_{Ohm}(\vec{r}, \omega) = \overleftrightarrow{\sigma}(\vec{r}, \omega)\vec{E}(\vec{r}, \omega)$ and $\vec{D}(\vec{r}, \omega) = \overleftrightarrow{\varepsilon}(\vec{r}, \omega)\vec{E}(\vec{r}, \omega)$. The magnitude $\vec{D}(\vec{r}, \omega)$ represents the electric displacement, and $\overleftrightarrow{\varepsilon}(\vec{r}, \omega)$ is the permittivity tensor for brain tissues. *Equations A1* imply that any mesoscopic volume inside the brain (e.g., a barrel) behaves like a multiple spatial filtering device with frequency characteristics depending notably on location and orientation. Bearing in mind that the maximum sampling rate used for standard LFP

observation is about 500 Hz, one must be careful when assuming that any ideal closed loop inside the tissue can be locally modeled as an ideal RC circuit. In such an imaginary loop, the total electric current in a particular region (*tissue A*) may be smaller than in an adjacent region (*tissue B*) within a particular frequency range ω_L [Fig. A1; i.e., $I_{A \to B}(\omega_L) \ll I_{B \to A}(\omega_L)$]. Thus, even though the actual total ohmic current, from where our LFP observations originate, is conserved within the loop and directly related to the impressed currents in each tissue region, for the observable frequency range it may apparently look like there are virtual either sources or sinks of electric current along the loop over time.

$$I_{\substack{A \to B \\ B \to A}}^{\text{Total}} = I_A^{\text{Impressed}} + I_B^{\text{Impressed}}$$

APPENDIX B: THE IONIC DIFFUSION PHENOMENON

As mentioned in the main text, the total electric current inside any mesoscopic brain area has usually been represented as the superposition of nondispersive ohmic electric currents $\vec{J}_{\text{Ohm}}(\vec{r},\ t) = \ddot{\sigma}(\vec{r})\vec{E}(\vec{r},\ t)$ and certain fictitious current sources $\vec{J}_p(\vec{r},\ t)$ that we refer to as "impressed." Hence, we ignore any contribution from ionic diffusion currents (Bédard and Destexhe 2009). In addition, the actual biophysical origin of $\vec{J}_p(\vec{r},\ t)$ is a set of transmembrane currents that results from temporal changes in the membrane permeability to certain ions, i.e., $\vec{J}_p(\vec{r},\ t)$ is created from strong electrochemical gradients across the cellular membranes.

Therefore, to have a proper formalization of the electrophysiological forward problem, it is necessary to have a term $\vec{J}_{\text{Diff}}(\vec{r},\ t)$ explicitly describing the diffusion of a variety of ions (*Eq. B1*) typically of different sizes (Li 2009). In this context, the impressed current source $\vec{J}_p(\vec{r},\ t)$ might irreversibly result from these ohmic and ionic diffusion currents in situations of thermodynamic disequilibrium.

$$\vec{J}_{\text{Total}}(\vec{r}, t) = \vec{J}_{\text{Ohm}}(\vec{r}, t) + \vec{J}_{\text{Diff}}(\vec{r}, t) \qquad (B1)$$

The total ionic diffusion current is defined as $\vec{J}_{\text{Diff}}(\vec{r},\ t) = \sum_i Fz_i\ \vec{f}_i(\vec{r},\ t)$, with the flux for each ion species given by Fick's first law, i.e., $\vec{f}_i(\vec{r},\ t) = -\ddot{D}_i(\vec{r})\nabla c_i(\vec{r},\ t)$ (Malmivuo and Plonsey 1995). The diffusion coefficient tensor $\ddot{D}_i(\vec{r}) = \ddot{u}_i(\vec{r})RT/|z_i|;F$ for each ion depends linearly on its mobility $\ddot{u}_i(\vec{r})$ (i.e., the Einstein-Smoluchowski relation). The ion charge number, temperature, and gas constant are represented by z_i, T, and R, respectively.

Under the conditions that the ions do not interact and that their concentrations are sufficiently low, the mesoscopic Maxwell equations for the propagation of the electromagnetic field in an electrolyte are, for the electric $\vec{E}(\vec{r},\ t)$ and displacement $\vec{D}(\vec{r},\ t)$ fields,

$$\nabla \cdot \vec{D}(\vec{r}, t) = \rho_{\text{Total}}(\vec{r}, t) \quad \text{Gauss's law} \qquad (B2a)$$

$$\nabla \cdot \vec{E}(\vec{r}, t) = -\frac{\partial \vec{B}(\vec{r}, t)}{\partial t} \quad \text{Faraday's law of induction} \quad (B2b)$$

and for the magnetic flux density $\vec{B}(\vec{r},\ t)$,

$$\nabla \cdot \vec{B}(\vec{r}, t) = 0 \ \to\ \vec{B}(\vec{r}, t) = \nabla \times \vec{A}(\vec{r}, t) \qquad (B2c)$$

$$\frac{\nabla \times \vec{B}(\vec{r}, t)}{\mu_0} = \vec{J}_{\text{Total}}(\vec{r}, t) + \frac{\partial \vec{D}(\vec{r}, t)}{\partial t} \quad \text{Ampere's law} \quad (B2d)$$

The magnitude $\vec{A}(\vec{r},\ t)$ is named the magnetic vector potential. At the frequency range of the electrophysiological phenomena, any magnetization of brain tissues has been historically ignored.

To warrant the conservation of the total charge $\nabla \cdot \vec{J}_{\text{Total}}(\vec{r},\ t) + \partial\rho_{\text{Total}}(\vec{r},\ t)/\partial t = 0$ whenever ionic diffusion processes are present, the Poison's law must include a term that describes ionic charge redistributions. The resulting Maxwell equation (*Eq. B2a*) is known as Poisson-Boltzmann's law (Grochowski and Trylska 2007). By defi-

Fig. A1. Schematic illustration of the first scenario for the CSD unbalance. A mesoscopic cortical region (i.e., a barrel) comprises 2 tissues, which could represent supragranular (*tissue A*) and infragranular (*tissue B*) layers. In the somatosensory cortex of rats, these layers have been found to have different conductivity values at 500 Hz (Goto et al. 2010). In addition, these tissues have different spectral characteristics for the electric conductivity (*left*), with the particularity that, for example, *tissue A* is less conductive than *tissue B* for the frequency range of the LFP. The total impressed currents generated by the neuronal activity in *tissues A* and *B* are $I_A^{\text{Impressed}}$ and $I_B^{\text{Impressed}}$, respectively. These impressed currents generate a total electric current flowing along a closed loop, with $I_{A \to B}^{\text{Total}}$ and $I_{B \to A}^{\text{Total}}$ for the respective sectors in each tissue. From Kirchhoff's current law, we must expect that $I_{A \to B}^{\text{Total}} = I_{B \to A}^{\text{Total}}$. However, the total ohmic current in each tissue separates into a component with low-frequency variations, which causes the LFP, and a nonobservable component with high-frequency variations. Even though the total ohmic current may be conserved, the low-frequency components could be different inside each tissue [$I_{A \to B}(\omega_L) \ll I_{B \to A}(\omega_L)$], giving the impression of some sites where the electric current is either created or annihilated.
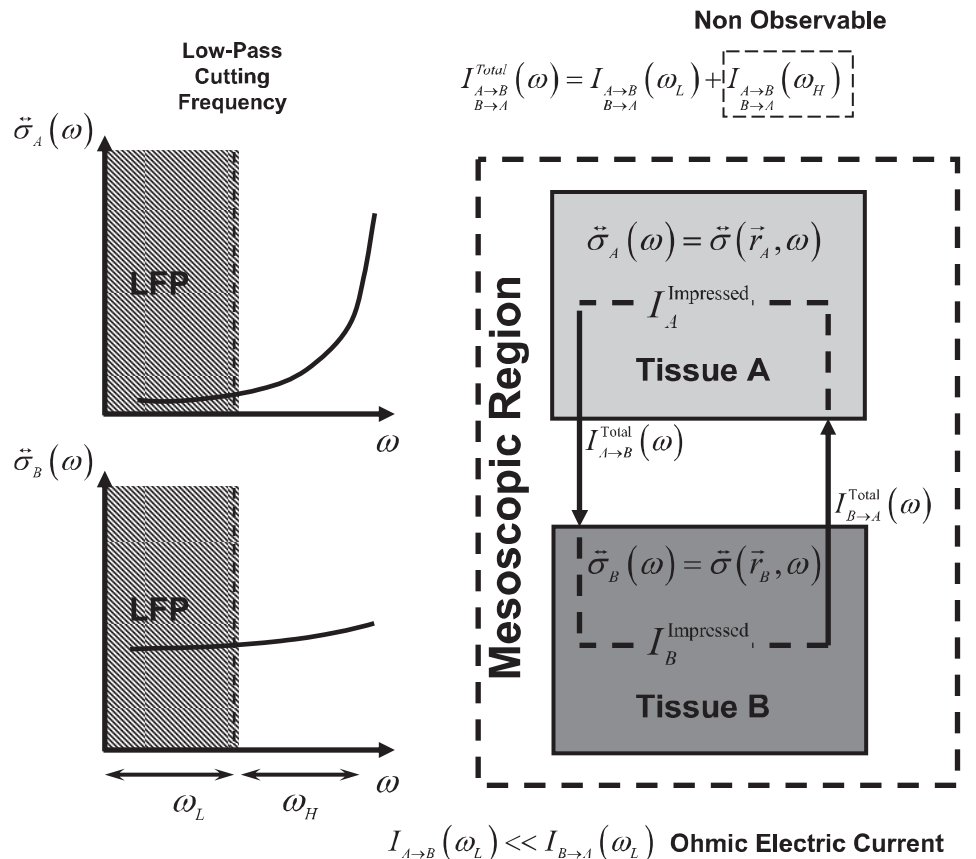
nition, the total charge density comprises a free and an ionic diffusion component, i.e., $\rho_{Total}(\vec{r}, t) = \rho_{Free}(\vec{r}, t) + \rho_{Ion}(\vec{r}, t)$, with $\rho_{Ion}(\vec{r}, t) = \sum_i Fz_i c_i(\vec{r}, t)$). Henceforth, let us consider for simplicity only the case of media both isotropic and with a single/instantaneous dielectric relaxation mechanism, i.e., $\overrightarrow{\mathbf{D}}(\vec{r}, t) = \varepsilon(\vec{r})\overrightarrow{\mathbf{E}}(\vec{r}, t)$ and $\overrightarrow{\mathbf{J}}_{Ohm}(\vec{r}, t) = \sigma(\vec{r})\overrightarrow{\mathbf{E}}(\vec{r}, t)$. Also, we are not interested in cases where a free charge density is created by particular distributions of macromolecules, i.e., we assume the free charge density is zero inside brain tissues.

Under a quasi-static approach (de Munck and van Dijk 1991; Plonsey and Heppner 1967), there are two main hypotheses about the propagation of electromagnetic field in biological tissues at low frequencies ($\omega \leq 10$ kHz), which are based on mean values (Hämäläinen 1993; Nunez and Srinivasan 2006) of the electric conductivity $\bar{\sigma} \approx 0.3$ S/m and permittivity $\bar{\varepsilon} \approx 10^5 \varepsilon_0$. The first hypothesis results from comparing the size of the mammalian head and the characteristic length $\lambda = [\mu_0 \omega^2 \bar{\varepsilon}(1 - i\bar{\sigma}/\omega\bar{\varepsilon})]^{-1/2} \approx 65$ m of the electromagnetic propagation wave. Consequently, any Faraday's induction effect is disregarded, i.e., $\nabla \cdot \overrightarrow{\mathbf{E}}(\vec{r}, t) = 0$, and the electric field is represented as a gradient of an electric potential $\overrightarrow{\mathbf{E}}(\vec{r}, t) = -\nabla\varphi(\vec{r}, t)$. At any location inside the brain, the displacement current is much smaller than the ohmic current, e.g., $(1 + i\omega\bar{\varepsilon}/\bar{\sigma}) \approx 1$, which constitutes the second hypothesis of the quasi-static approach. Therefore, the mesoscopic Maxwell equations for such a particular case are

$$-\nabla \cdot \left(\varepsilon(\vec{r}) \nabla \varphi(\vec{r}, t) \right) = \sum_i Fz_i c_i(\vec{r}, t) \qquad (B3a)$$

$$\frac{\nabla \times \nabla \times \vec{A}(\vec{r}, t)}{\mu_0} = -\sigma(\vec{r}) \nabla \varphi(\vec{r}, t) - \sum_i Fz_i D_i(\vec{r}) \nabla c_i(\vec{r}, t) \qquad (B3b)$$

On the other hand, as a consequence of electrochemical gradients $\mu_i(\vec{r}, t)$ in the brain tissues, the total ionic flux for each species is determined by the sum of diffusion and electrical current components.

$$\vec{\mathbf{j}}_i(\vec{r}, t) = -\frac{D_i(\vec{r})c_i(\vec{r}, t)}{RT} \nabla \mu_i(\vec{r}, t) \qquad (B4)$$

$$\mu_i(\vec{r}, t) = \mu_i^0 + RT \log(c_i(\vec{r}, t)) + Fz_i\varphi(\vec{r}, t) \qquad (B5)$$

Based on the mass conservation law for each ion, i.e., $\nabla \cdot \vec{\mathbf{j}}_i(\vec{r}, t) = -[\partial c_i(\vec{r}, t)/\partial t]$, its concentration in the tissue must obey the following equation:

$$\frac{\partial c_i(\vec{r}, t)}{\partial t} = \nabla \cdot \left[D_i(\vec{r}) \left(\nabla c_i(\vec{r}, t) + \frac{Fz_i c_i(\vec{r}, t)}{RT} \nabla \varphi(\vec{r}, t) \right) \right] \qquad (B6)$$

Equations B3a and *B6* together constitute the classical Poisson-Boltzmann-Nernst-Planck model (Zheng and Wei 2011).

Let us assume that, as a result of the neuronal activity, there are timely changes in the transmembrane mobility to certain ions $u_i(\vec{r})$. These changes will cause the emergence of impressed current sources $\vec{\mathbf{J}}_p(\vec{r}, t) = \sum_{i\in\Theta} Fz_i \vec{\mathbf{J}}_i(\vec{r}, t)$ which might include both ohmic and ionic diffusion components.

$$\frac{\partial c_i(\vec{r}, t)}{\partial t} = \nabla \cdot \left[D_i(\vec{r}) \left(\nabla c_i(\vec{r}, t) + \frac{Fz_i c_i(\vec{r}, t)}{RT} \nabla \varphi(\vec{r}, t) \right) \right] - \nabla \cdot \vec{\mathbf{j}}_i(\vec{r}, t) \qquad (B7a)$$

$$\frac{\nabla \times \nabla \times \vec{A}(\vec{r}, t)}{\mu_0} = -\sigma(\vec{r}) \nabla \varphi(\vec{r}, t) + \sum_i Fz_i D_i(\vec{r}) \nabla c_i(\vec{r}, t) + \vec{\mathbf{J}}_P(\vec{r}, t) \qquad (B7b)$$

Under the validity of the Nernst-Planck electroneutrality condition, *Eqs. B7a* and *B7b* are equivalent, with the total conductivity $\sigma(\vec{r}) =$
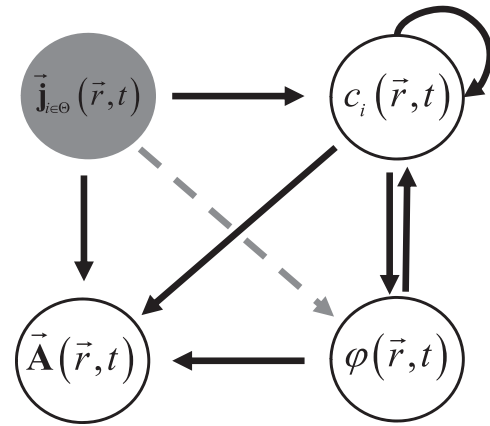
Fig. B1. Schematic illustration of the second scenario for the CSD unbalance, showing the general cause-effect flow (causes, shaded circle; effect, open circles) in the electrophysiological forward problem when ionic diffusion mechanisms are included. See APPENDIX B for definitions.

$\sum_i Fz_i u_i(\vec{r})\hat{c}_i(\vec{r})$ defined from mean values $\hat{c}_i(\vec{r})$ of the ion concentrations over time (Giebish et al. 1978).

The cause-effect flow diagram for the general system of equations, i.e., *Eqs. B3a* and *B7*, is shown in Fig. B1.

DISCLOSURES

No conflicts of interest, financial or otherwise, are declared by the authors.

AUTHOR CONTRIBUTIONS

Author contributions: J.J.R. conception and design of research; J.J.R., T.O., T.G., A.S., and H.N. performed experiments; J.J.R., T.O., and T.G. analyzed data; J.J.R., A.E., H.M., and R.K. interpreted results of experiments; J.J.R., T.O., and T.G. prepared figures; J.J.R. drafted manuscript; J.J.R. edited and revised manuscript; J.J.R., T.O., T.G., A.S., H.N., A.E., H.M., and R.K. approved final version of manuscript.

REFERENCES

Abraham K, Ajmone-Marsan C. Patterns of cortical discharges and their relation to routine scalp electroencephalography. *Electroencephalogr Clin Neurophysiol* 10: 447–461, 1958.

Adrian ED, Matthews BHC. The Berger rhythm: potential changes from the occipital lobes in man. *Brain* 57: 355–385, 1934.

Ahrens KF, Kleinfeld D. Current flow in vibrissa motor cortex can phase-lock with exploratory rhythmic whisking in Rat. *J Neurophysiol* 92: 1700–1707, 2004.

Baillet S, Mosher JC, Leahy RM. Electromagnetic brain mapping. *IEEE Signal Process Mag* 18: 14–30, 2001.

Bédard C, Destexhe A. Macroscopic models of local field potentials and the apparent 1/*f* noise in brain activity. *Biophys J* 96: 2589–2603, 2009.

Beevers CA. On the interpretation of electroencephalic potentials. *Proc R Soc Edinburgh B Biol* 62: 43–50, 1944.

Bereshpolova Y, Amitai Y, Gusev AG, Stoelzel CR, Swadlow HA. Dendritic backpropagation and the state of the awake neocortex. *J Neurosci* 27: 9392–9399, 2007.

Berger H. Über das Elektroenkephalogramm des Menschen. *Arch Psychiatr Nervenkr* 87: 527–570, 1929.

Bertrand O, Perrin F, Pernier J. A theoretical justification of the average reference in topographic evoked potential studies. *Electroencephalogr Clin Neurophysiol* 62: 462–464, 1985.

Boorman L, Kennerley AN, Johnston D, Jones M, Zheng Y, Redgrave P, Berwick J. Negative blood oxygen level dependence in the rat: a model for investigating the role of suppression in neurovascular coupling. *J Neurosci* 30: 4285–4294, 2010.

Bowyer SM, Okada YC, Papuashvili N, Moran JE, Barkley GL, Welch KMA, Tepley N. Analysis of MEG signals of spreading cortical depression with propagation constrained to a rectangular cortical strip. I. Lissencephalic rabbit model. *Brain Res* 843: 71–78, 1999.

Brankačˇk J, Stewart M, Fox SE. Current source density analysis of the hippocampal theta rhythm: associated sustained potentials and candidate synaptic generators. *Brain Res* 615: 310–327, 1993.

Brazier MAB. The electrical fields at the surface of the head during sleep. *Electroencephalogr Clin Neurophysiol* l: 195–204, 1949.

Buzsáki G, Kandel A. Somadendritic backpropagation of action potentials in cortical pyramidal cells of the awake rat. *J Neurophysiol* 79: 1587–1591, 1998.

Calvet J, Calvet MC, Scherrer J. Étude stratigraphique corticale de l'activité: EEG spontanée. *Electroencephalogr Clin Neurophysiol* 17: 109–125, 1964.

Calvet J, Scherrer J. Activité bioélectrique de l'écorce cérébrale á ses différents niveaux. *CR Seances Soc Biol Fil* 155: 275–278, 1961.

Chapman RM, Ilmoniemi RJ, Barbanera S, Romani GL. Selective localization of alpha brain activity with neuromagnetic measurements. *Electroencephalogr Clin Neurophysiol* 58: 569–572, 1984.

Cohen D, Cuffin BN. Demonstrations of useful differences between magnetoencephalogram and electroencephalogram. *Electroencephalogr Clin Neurophysiol* 56: 38–51, 1983.

Cooper R, Winter AL, Crow HJ, Grey Walter W. Comparison of subcortical, cortical and scalp activity using chronically indwelling electrodes in man. *Electroencephalogr Clin Neurophysiol* 18: 217–228, 1965.

de Celis Alonso B, Lowe AS, Dear JP, Lee KC, Williams SCR, Finnerty GT. Sensory inputs from whisking movements modify cortical whisker maps visualized with functional magnetic resonance imaging. *Cereb Cortex* 18: 1314–1325, 2008.

de Munck JC, van Dijk BW. Symmetry considerations in the quasi-static approximation of volume conductor theory. *Phys Med Biol* 36: 521–529, 1991.

Dehghani N, Bédard C, Cash SS, Halgren E, Destexhe A. Comparative power spectral analysis of simultaneous electroencephalographic and magnetoencephalographic recordings in humans suggests non-resistive extracellular media. *J Comput Neurosci* 29: 405–421, 2011.

Di S, Baumgartner C, Barth D. Laminar analysis of the extracellular field potentials in rat vibrissa/barrel cortex. *J Neurophysiol* 63: 832–840, 1990.

Ebersole JS. Defining epileptogenic foci: past, present, future. *J Clin Neurophysiol* 14: 470–483, 1997.

Ebersole JS. Noninvasive localization of epileptogenic foci by EEG source modeling. *Epilepsia* 41: S24–S33, 2000.

Ferezou I, Haiss F, Gentet LJ, Aronoff R, Weber B, Petersen CCH. Spatiotemporal dynamics of cortical sensorimotor integration in behaving mice. *Neuron* 56: 907–923, 2007.

Fernandes JM, Martins da Silva A, Huiskamp G, Velis DN, Manshanden I, de Munck JC, Lopes da Silva F, Silva Cunha JP. What does an epileptiform spike look like in MEG? Comparison between coincident EEG and MEG spikes. *J Clin Neurophysiol* 22: 68–73, 2005.

Freeman WJ. Distribution in time and space of prepyriform electrical activity. *J Neurophysiol* 22: 644–665, 1959.

Freeman WJ. *Mass Action in the Nervous System.* New York: Academic, 1975, p. 454.

Gabriel S, Lau RW, Gabriel C. The dielectric properties of biological tissues: II. Measurements in the frequency range 10 Hz to 20 GHz. *Phys Med Biol* 41: 2251–2269, 1996.

Gabriel C, Peyman A, Grant EH. Electrical conductivity of tissue at frequencies below 1 MHz. *Phys Med Biol* 54: 4863–4878, 2009.

Giebisch G, Tosteson DC, Ussing HH, Tosteson MT. *Membrane Transport in Biology. I. Concepts and Models.* Berlin: Springer, 1978.

Gold C, Henze DA, Koch C. Using extracellular action potential recordings to constrain compartmental models. *J Comput Neurosci* 23: 39–58, 2007.

Gold C, Henze DA, Koch C, Buzsáki G. On the origin of the extracellular action potential waveform: a modeling study. *J Neurophysiol* 95: 3113–3128, 2006.

Goto T, Hatanaka R, Ogawa T, Sumiyoshi A, Riera J, Kawashima R. An evaluation of the conductivity profile in the barrel cortex of Wistar rats. *J Neurophysiol* 104: 3388–3412, 2010.

Goto T, Ogawa T, Riera J, Kawashima R. Localization of single barrel column by means of a volumetric current source density analysis in the somatosensory cortex of rat. *Neurosci Res* 71, *Suppl*: e304–e305, 2011.

Grochowski P, Trylska J. Continuum molecular electrostatics, salt effects, and counterion binding. A review of the Poisson-Boltzmann theory and its modifications. *Biopolymers* 89: 93–113, 2007.

Gumnit R, Takahashi T. Changes in direct current activity during experimental focal seizures. *Electroencephalogr Clin Neurophysiol* 19: 63–74, 1965.

Hämäläinen M, Hari R, Ilmoniemi R, Knuutila J, Lounasmaa O. Magnetoencephalography—theory, instrumentation and applications to the noninvasive study of human brain function. *Rev Mod Phys* 65: 413–497, 1993.

Hämäläinen M, Ilmoniemi R. *Interpreting Measured Magnetic Fields of the Brain: Estimates of Current Distributions.* Report TKK-F-A559. Helsinki University of Technology, Espoo, Finland, 1984.

Hämäläinen MS, Sarvas J. Realistic conductivity geometry model of the human head for interpretation of neuromagnetic data. *IEEE Trans Biomed Eng* 36: 165–171, 1989.

Hari R, Ilmoniemi R. Cerebral magnetic fields. *Crit Rev Biomed Eng* 14: 93–126, 1986.

Henderson CJ, Butler SR, Glass A. The localization of equivalent dipoles of EEG sources by the application of electrical field theory. *Electroencephalogr Clin Neurophysiol* 39: 117–130, 1975.

Higley MJ, Contreras D. Cellular mechanisms of suppressive interactions between somatosensory responses in vivo. *J Neurophysiol* 97: 647–658, 2007.

Holt GR, Koch C. Electrical interactions via the extracellular potential near cell bodies. *J Comput Neurosci* 6: 169–184, 1999.

Huiskamp G, van der Meij W, van Huffelen A, van Nieuwenhuizen O. High resolution spatio-temporal EEG-MEG analysis of Rolandic spikes. *J Clin Neurophysiol* 21: 84–95, 2004.

Humphrey DR. Re-analysis of the antidromic cortical response. I. Potentials evoked by stimulation of the isolated pyramidal tract. *Electroencephalogr Clin Neurophysiol* 24: 116–129, 1968.

Jerbi K, Mosher JC, Baillet S, Leahy RM. On MEG forward modelling using multipolar expansions. *Phys Med Biol* 47: 523–555, 2002.

Johnston D, Wu SMS. *Foundations of Cellular Neurophysiology* (1st ed.). Cambridge, MA: MIT Press, 1995.

Jones SR, Pritchett DL, Sikora MA, Stufflebeam SM, Hämäläinen M, Moore CI. Quantitative analysis and biophysically realistic neural modeling of the MEG mu rhythm: rhythmogenesis and modulation of sensory-evoked responses. *J Neurophysiol* 102: 3554–3572, 2009.

Jones SR, Pritchett DL, Stufflebeam SM, Hämäläinen M, Moore CI. Neural correlates of tactile detection: a combined magnetoencephalography and biophysically based computational modeling study. *J Neurosci* 27: 10751–10764, 2007.

Kennedy JL, Gottsdanker RM, Armington JC, Gray FE. A new electroencephalogram associated with thinking. *Science* 108: 527–529, 1948.

Klee M, Rall W. Computed potentials of cortically arranged populations of neurons. *J Neurophysiol* 40: 647–666, 1977.

Kraut MA, Arezzo JC, Vaughan HG. Intracortical generators of the flash VEP in monkeys. *Electroencephalogr Clin Neurophysiol* 62: 300–312, 1985.

Lakatos P, Chen CM, O'Connell MN, Mills A, Schroeder CE. Neuronal oscillations and multisensory interaction in primary auditory cortex. *Neuron* 53: 279–292, 2007.

Lakatos P, Karmos G, Mehta AD, Ulbert I, Schroeder CE. Entrainment of neuronal oscillations as a mechanism of attentional selection. *Science* 320: 110–113, 2008.

Li B. Continuum electrostatics for ionic solutions with non-uniform ionic sizes. *Nonlinearity* 22: 811–833, 2009.

Li CL, Bak AF, Parker LO. Specific resistivity of the cerebral cortex and white matter. *Exp Neurol* 20: 544–557, 1968.

Llinás RR, Nicholson C. Analysis of field potential in the central nervous system. In: *Basic Neurophysiology of Neuronal and Glial Potentials. Handbook of Electroencephalogr Clin Neurophysiol.* Amsterdam: Elsevier, 1974, p. 61–84.

Lopes da Silva FH, Van Leeuwen WS. The cortical source of the alpha rhythm. *Neurosci Lett* 6: 237–241, 1977.

Lorente de Nó R. Analysis of the distribution of the action currents of nerve in volume conductors. *Stud Rockefeller Inst Med Res Repr* 132: 384–477, 1947.

Malmivuo J, Plonsey R. *Bioelectromagnetism Principles and Applications of Bioelectric and Biomagnetic Fields.* New York: Oxford University Press, 1995.

Mégevand P, Quairiaux C, Lascano AM, Kiss JZ, Michel CM. A mouse model for studying large-scale neuronal networks using EEG mapping techniques. *Neuroimage* 42: 591–602, 2008.

Mikuni N, Nagamine T, Ikeda A, Terada K, Taki W, Kimura J, Kikuchi H, Shibasaki H. Simultaneous recording of epileptiform discharges by MEG and subdural electrodes in temporal lobe epilepsy. *Neuroimage* 5: 298–306, 1997.

Milstein JN, Koch C. Dynamic moment analysis of the extracellular electric field of a biologically realistic spiking neuron. *Neural Comput* 20: 2070–2084, 2008.

Mosher JC, Lewis PS, Leahy RM. Multiple dipole modeling and localization from spatio-temporal MEG data. *IEEE Trans Biomed Eng* 39: 541–557, 1992.

Murakami S, Okada Y. Contributions of principal neocortical neurons to magnetoencephalography and electroencephalography signals. *J Physiol* 575: 925–936, 2006.

Murakami S, Zhang T, Hirose A, Okada YC. Physiological origins of evoked magnetic fields and extracellular field potentials produced by guinea-pig CA3 hippocampal slices. *J Physiol* 544: 237–251, 2002.

Niedermeyer E, Lopes da Silva F. *Electroencephalography: Basic Principles. Clinical Applications and Related Fields* (2nd ed.). Baltimore, MD: Urban and Schwarzenberg, 1987.

Nunez PL. *Electric Fields of the Brain.* New York: Oxford University Press, 1981.

Nunez P, Srinivasan R. *Electric Fields of the Brain. The Neurophysics of EEG* (2nd ed.). New York: Oxford University Press, 2006.

Ogawa T, Riera J, Goto T, Sumiyoshi A, Nonaka H, Jerbi K, Bertrand O, Kawashima R. Large-scale heterogeneous representation of sound attributes in rat primary auditory cortex: from unit activity to population dynamics. *J Neurosci* 31: 14639–14653, 2011.

Oishi M, Otsubo H, Kameyama S, Morota N, Masuda H, Kitayama M, Tanaka R. Epileptic spikes: magnetoencephalography versus simultaneous electrocorticography. *Epilepsia* 43: 1390–1395, 2002.

Okada YC, Wu J, Kyuhou S. Genesis of MEG signals in a mammalian CNS structure. *Electroencephalogr Clin Neurophysiol* 103: 474–485, 1997.

Oostendorp T, Delbeke J, Stegeman DF. The conductivity of human skull: results of in vivo and in vitro measurements. *IEEE Trans Biomed Eng* 47: 1487–1492, 2000.

Pascual-Marqui RD. Review of methods for solving the EEG inverse problem. *Int J Bioelectromagn* 1: 75–86, 1999.

Paxinos G, Watson C. *The Rat Brain in Stereotaxic Coordinates* (6th ed.). Burlington, VT: Academic, 2007.

Petersen CCH. The functional organization of the barrel cortex. *Neuron* 56: 339–355, 2007.

Petsche H, Prohaska O, Rappelsberger P, Vollmer R, Pockberger H. Simultaneous laminar intracortical recordings in seizures. *Electroencephalogr Clin Neurophysiol* 42: 414–416, 1977.

Pettersen K, Devor A, Ulbert I, Dale AM, Einevoll GT. Current-source density estimation based on inversion of electrostatic forward solution: effects of finite extent of neuronal activity and conductivity discontinuities. *J Neurosci Methods* 154: 116–133, 2006.

Pettersen KH, Einevoll GT. Amplitude variability and extracellular low-pass filtering of neuronal spikes. *Biophys J* 94: 784–802, 2008.

Plonsey R. *Bioelectric Phenomena.* New York: McGraw-Hill, 1969.

Plonsey R, Heppner DB. Considerations of quasi-stationarity in electrophysiological systems. *Bull Math Biophys* 29: 657–664, 1967.

Pollen DA. On the generation of neocortical potentials. In: *Basic Mechanisms of the Epilepsies*, edited by Jasper HH, Ward AA, and Pope A. Boston, MA: Little, Brown, 1969, p. 411–420.

Rall W. Electrophysiology of a dendritic neuron model. *Biophys J* 2: 145–167, 1962.

Ranck JB Jr. Specific impedance of rabbit cerebral cortex. *Exp Neurol* 7: 144–152, 1963.

Rappelsberger P, Pockberger H, Petsche H. The contribution of the cortical layers to the generation of the EEG field potential and current source density analyses in the rabbit's visual cortex. *Electroencephalogr Clin Neurophysiol* 53: 254–269, 1982.

Riera J, Ogawa T, Hatanaka R, Goto T, Sumiyoshi A, Enjieu-Kadji H, Nakauchi S, Kawashima R. Concurrent observations of astrocytic Ca^{2+} activity and multi-site extracellular potentials from an intact cerebral cortex. *J Biophotonics* 3: 147–160, 2010a.

Riera JJ, Aubert E, Valdes-Sosa P, Casanova R, Lins O. Discrete spline electric-magnetic tomography (DSPECT) based on realistic neuroanatomy. In: *Biomag 96. Proceedings of the Tenth International Conference on Biomagnetism.* New York: Springer, 2000, p. 326–329.

Riera JJ, Jimenez JC, Wan X, Kawashima R, Ozaki T. Nonlinear local electro-vascular coupling. Part II: From data to neural masses. *Hum Brain Mapp* 28: 335–354, 2007.

Riera JJ, Schousboe A, Waagepetersen HS, Howarth C, Hyder F. The micro-architecture of the cerebral cortex: Functional neuroimaging models and metabolism. *Neuroimage* 40: 1436–1459, 2008.

Riera JJ, Sumiyoshi A, Kawashima R. *MRI Compatible Mini-cap for EEG Recordings From Rodents.* Patent application no. JP 2010-983220, Japan, 2010b.

Riera JJ, Wan X, Jimenez JC, Kawashima R. Nonlinear local electro-vascular coupling. Part I: A theoretical model. *Hum Brain Mapp* 27: 896–914, 2006.

Scherg M, Von Cramon D. Two bilateral sources of the late AEP as identified by a spatio-temporal dipole model. *Electroencephalogr Clin Neurophysiol* 62: 32–44, 1985.

Schneider MR. A multistage process for computing virtual dipolar sources of EEG discharges from surface information. *IEEE Trans Biomed Eng* BME-19: 1–12, 1972.

Sem-Jacobsen CW, Petersen MC, Lazarte JA, Dodge HW, Holman CB. Electroencephalographic rhythms from depths of the frontal lobe in 60 psychotic patients. *Electroencephalogr Clin Neurophysiol* 7: 193–210, 1955.

Shaw JC, Roth M. Potential distribution analysis. II: A theoretical consideration of its significance in terms of electric field theory. *Electroencephalogr Clin Neurophysiol* 7: 285–292, 1955.

Shu Y, Hasenstaub A, Duque A, Yu Y, McCormick DA. Modulation of intracortical synaptic potentials by presynaptic somatic membrane potential. *Nature* 441: 761–765, 2006.

Sumiyoshi A, Riera JJ, Ogawa T, Kawashima R. A mini-cap for simultaneous EEG and fMRI recording in rodents. *Neuroimage* 54: 1951–1965, 2011.

Tao JX, Ray A, Hawes-Ebersole S, Ebersole JS. Intracranial EEG substrates of scalp EEG interictal spikes. *Epilepsia* 46: 669–676, 2005.

Traub RD, Wong RKS, Miles R, Michelson H. A model of a CA3 hippocampal pyramidal neuron incorporating voltage-clamp data on intrinsic conductances. *J Neurophysiol* 66: 635–650, 1991.

Walter WG, Walter VJ. The electrical activity of the brain. *Annu Rev Physiol* 11: 199–230, 1949.

Xu XL, Xu B, He B. An alternative subspace approach to EEG dipole source localization. *Phys Med Biol* 49: 327–343, 2004.

Zheng Q, Wei GW. Poisson-Boltzmann-Nernst-Planck model. *J Chem Phys* 134, 194101, 2011.